

Vortex dynamics in three-dimensional continuous myocardium with fiber rotation: Filament instability and fibrillation^{a)}

Flavio Fenton and Alain Karma

*Department of Physics and Center for Interdisciplinary Research on Complex Systems,
Northeastern University, Boston, Massachusetts 02115*

(Received 19 August 1997; accepted for publication 21 November 1997)

Wave propagation in ventricular muscle is rendered highly anisotropic by the intramural rotation of the fiber. This rotational anisotropy is especially important because it can produce a twist of electrical vortices, which measures the rate of rotation (in degree/mm) of activation wavefronts in successive planes perpendicular to a line of phase singularity, or filament. This twist can then significantly alter the dynamics of the filament. This paper explores this dynamics via numerical simulation. After a review of the literature, we present modeling tools that include: (i) a simplified ionic model with three membrane currents that approximates well the restitution properties and spiral wave behavior of more complex ionic models of cardiac action potential (Beeler-Reuter and others), and (ii) a semi-implicit algorithm for the fast solution of monodomain cable equations with rotational anisotropy. We then discuss selected results of a simulation study of vortex dynamics in a parallelepipedal slab of ventricular muscle of varying wall thickness (S) and fiber rotation rate (θ_z). The main finding is that rotational anisotropy generates a sufficiently large twist to destabilize a single transmural filament and cause a transition to a wave turbulent state characterized by a high density of chaotically moving filaments. This instability is manifested by the propagation of localized disturbances along the filament and has no previously known analog in isotropic excitable media. These disturbances correspond to highly twisted and distorted regions of filament, or “twistons,” that create vortex rings when colliding with the natural boundaries of the ventricle. Moreover, when sufficiently twisted, these rings expand and create additional filaments by further colliding with boundaries. This instability mechanism is distinct from the commonly invoked patchy failure or wave breakup that is not observed here during the initial instability. For modified Beeler-Reuter-like kinetics with stable reentry in two dimensions, decay into turbulence occurs in the left ventricle in about one second above a critical wall thickness in the range of 4–6 mm that matches experiment. However this decay is suppressed by uniformly decreasing excitability. Specific experiments to test these results, and a method to characterize the filament density during fibrillation are discussed. Results are contrasted with other mechanisms of fibrillation and future prospects are summarized. © 1998 American Institute of Physics. [S1054-1500(98)02201-0]

Ventricular fibrillation (VF) is a disorganized electrical wave activity that destroys the coherent contraction of the ventricular muscle and its main pumping function. Progress to date has led to the plausible hypothesis that the underlying mechanism of VF are “electrical vortices,” which are topological analogs of the hydrodynamic point vortices and vortex filaments present in a turbulent fluid, and manifested in the heart as spiral waves (in two dimensions) and scroll waves (in three dimensions) of action potential. A fair amount is known about how vortex filaments behave in a generic “isotropic” excitable media where waves propagate with the same speed in all directions. However, much less is known about their behavior in bulk ventricular muscle where waves propagate faster parallel to the fibers than perpendicular to them and the fiber axis rotates transmurally across the ventricle. This paper studies the effect of this rotation on the dynamics of vortex filaments by numerical simulation of electrical

impulse propagation in a slab of tissue. The main finding is that this anisotropy produces a new type of twist-induced filament instability that can cause a transition to wave turbulence. This instability is characterized by distortions that travel along the filament similarly to solitons along hydrodynamic vortex lines and cause filaments to multiply by repeated collisions with boundaries.

I. INTRODUCTION

Spiral and scroll waves have been extensively studied in recent years because of their central role in understanding arrhythmogenesis in cardiac tissue.^{1–3} These waves provide a plausible explanation for the creation of reentrant pathways of electrical activity around a point (in 2D) or line (in 3D) of phase singularity, which are dynamically generated but not preexistent in the tissue. This pathological behavior, broadly described as “functional” reentry in the cardiology literature, differs from “anatomical” reentry that involves propagation around some fixed preexisting obstacle, and is topologically simply analogous to plane wave propagation. Spiral

^{a)}Research supported by the American Heart Association.

and scroll waves have a typical rotation period in the range of 100–200 ms, which is shorter than the basic period of pacemaker cells and can therefore lead to an abnormally rapid heart beat or tachycardia. In a healthy heart, ventricular tachycardia (VT) usually degenerates into ventricular fibrillation (VF) after a short period of a few seconds, whereas in a diseased heart stable forms of anatomical VTs can sometimes be sustained because of preexistent regions of damaged tissue. A fundamental understanding of VF remains an essential prerequisite for improving current methods of defibrillation,⁴ developing possible alternatives to massive defibrillatory shocks based on spatiotemporal control of vortices,⁵ as well as designing drug therapies to reduce vulnerability to VF.

At present, our understanding of this transition in either healthy or diseased tissue remains largely speculative. Mapping methods, using voltage sensitive dye^{6–8} or large arrays of recording electrodes,^{9,10} permit to visualize the wave activity at the surface of the muscle, but not directly in its interior. This makes it difficult to pinpoint experimentally what type of wave instability causes VT to decay into VF after a few rotation periods. Moreover, from a purely modeling standpoint, it has remained difficult to quantitatively simulate reentry in a 3D *continuous* tissue. This is due both to the complexity of ionic models that describe ventricular action potential,^{11–15} and to the extreme abruptness of excitation (i.e., depolarization of the membrane) that occurs over a ms time scale. The fact that this time scale is much shorter than the action potential duration, typically ~ 100 – 200 ms, renders the partial differential equations describing wave propagation¹⁶ extremely stiff and difficult to solve. As a result, even very basic questions concerning the dynamics of reentry in ventricular muscle have remained unanswered.

In this paper we focus on the following basic set of related questions: What is the motion of vortex filaments in the presence of the intramural fiber rotation inherent in the architecture of ventricular muscle? Are transmural filaments morphologically stable, remaining roughly straight, or can they adopt more convoluted shapes? Moreover, can twist produce an instability of such filaments that leads to VF for physiologically plausible parameter ranges where spiral waves (rotors) are stable in 2D? If so, what is the precise mechanism of this instability and under what conditions (wall thickness, fiber rotation rate...) will it occur?

In Sec. II we review the experimental and theoretical literature related to these questions. We define rotational anisotropy and describe how it modifies the spread of excitation as a simple illustrative example. We then introduce the concept of vortex line (filament) and twist. We review some of the known effects of twist on the dynamics of scroll waves in isotropic excitable media that are potentially relevant for myocardium and VF.

The rest of this paper is then devoted to present modeling tools to address the questions above and to discuss some of the basic answers that we have obtained so far. In Sec. III, we write down the basic cable equations of propagation in continuous myocardium with rotational anisotropy and we present an efficient numerical algorithm to solve these equations. In Sec. IV we describe a simplified ionic model of

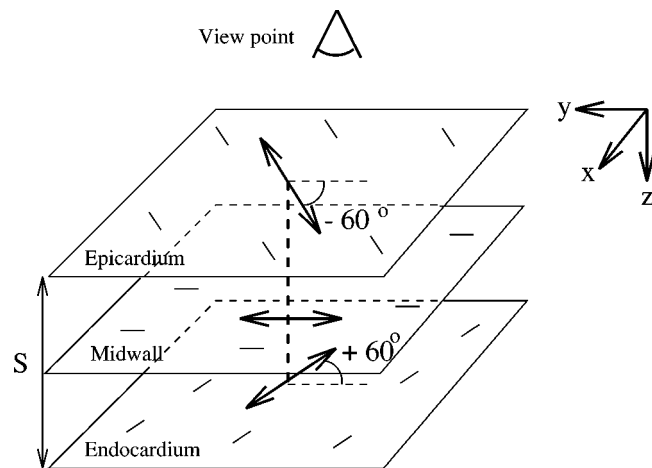


FIG. 1. Schematic representation of a parallelepipedal slab of ventricular muscle of wall thickness S showing the fiber pattern on the epicardium, midwall, and endocardium, and the continuous rotation of the fiber axis by $\Delta\theta = 120^\circ$.

ventricular action potential that incorporates quantitatively the restitution properties (action potential duration and conduction velocity) of more complex ionic models such as Beeler-Reuter,¹² or experimentally measured restitution curves.^{17–19} The validation of this simplified model is described in Sec. V where it is shown that it reproduces faithfully the two-dimensional patterns of reentry of the more complex models. The issue of whether any of the current ionic models reproduces the reentry patterns observed experimentally is also addressed in this section. The concrete output of the tools developed in Secs. III and IV is to make it possible to simulate a few seconds of modified Beeler-Reuter-like reentry in a parallelepipedal slab of ventricular tissue of typical dimension $\approx 6 \times 6 \times 1$ cm; and hence to study quantitatively the effect of rotational anisotropy on the stability of three-dimensional reentry. In Sec. VI we deal with the practical issue of characterizing the twist of meandering vortex lines. The most relevant simulation results are then presented in Sec. VII. They are discussed and compared to other works in Sec. VIII where the limitations of this study and future prospects are also summarized. Conclusions are given in Sec. IX.

We have found it best to write this paper in such a way that it is self-contained, even though certain modeling aspects and results will be exposed in more details elsewhere. In particular, the numerical algorithm is described here in its entirety and the basic equations and parameters of the simplified ionic model are written down with sufficient details to allow the interested reader to reproduce all the present computations.

II. REVIEW

A. Rotational anisotropy

The structure of ventricular muscle has been characterized through meticulous structural studies.^{20–22} For an idealized parallelepipedal slab of muscle, the fiber axis rotates continuously between the two bounding surfaces of the muscle as shown schematically in Fig. 1. Some of the im-

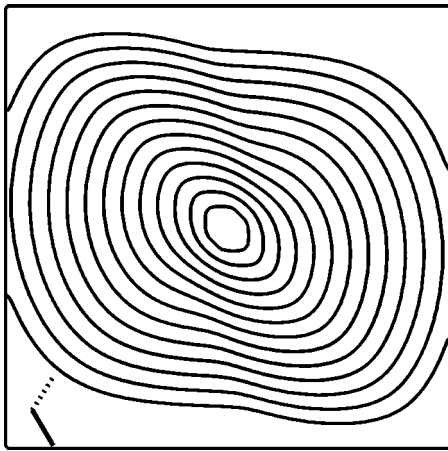


FIG. 2. Isochrone lines spaced every 5 ms in time showing the spread of excitation on the epicardium in response to a point stimulus at the center of the epicardium. Results are obtained by simulation of a three-current ionic model that closely approximates Beeler-Reuter kinetics. Spread takes place in a parallelepipedal slab of dimension $4 \times 4 \times 0.25$ cm with $\Delta\theta = 120^\circ$, $c_{\parallel} = 42$ cm/s, and $c_{\perp 1} = c_{\perp 2} = 18.7$ cm/s. The fiber direction is shown on the epicardium (solid line-segment) and the endocardium (dashed line-segment).

portant features are that: (i) The cells are shaped as flattened tubes, about $80\text{--}100\ \mu\text{m}$ long, with roughly elliptic cross sections with a major axis of $10\text{--}20\ \mu\text{m}$. (ii) They are arranged in sheets roughly parallel to the surfaces (epicardium and endocardium) of the muscle. (iii) The fiber axis (long axis of the cells) rotates continuously between the top and bottom sheets by an angle $\Delta\theta$, and the rotation is counter-clockwise from epicardium to endocardium as viewed from the top of the epicardium.

Peskin²³ has attempted to derive the fiber architecture of the heart from first principles of mechanics. His analysis predicts that $\Delta\theta = 180^\circ$, whereas dissection studies often report a smaller rotation angle in the range of $100^\circ\text{--}120^\circ$, some rotation being lost near the surface. Independently of its magnitude, which is at least greater than 100° according to both theory and experiment, this angle is roughly constant throughout the ventricles. Consequently, the fiber rotation rate $\theta_z \equiv \Delta\theta/S$, where S is the wall thickness, is larger in the right ventricle (RV), where $S \approx 2\text{--}4$ mm, than in the left ventricle (LV), where $S \approx 1\text{--}2$ cm. Activation wavefronts propagate two to three times faster parallel to the fiber axis than perpendicular to it. It is therefore useful to distinguish three conduction velocities: parallel to the fiber axis, c_{\parallel} , perpendicular to this axis in the plane of the fibers, $c_{\perp 1}$, and perpendicular to this plane (transmurally), $c_{\perp 2}$. In the continuous cable theory described in Sec. III, this rotational anisotropy is described by a conductivity tensor that renders modeling more difficult than in an isotropic medium.

B. Effect of rotational anisotropy on the spread of excitation: A simple example

The spread of an excitation wavefront in bulk myocardial tissue has been studied fairly extensively.^{24–27} It is worthwhile to briefly discuss this spread here since it provides basic intuition into the effect of fiber rotation on wave propagation. For this purpose, we have shown in Fig. 2 the

results of a simulation of the spread of excitation in the idealized geometry of a Fig. 1, i.e., an idealized parallelepipedal slab of muscle, with a point stimulus placed at the center of the epicardium. The resulting isochrone pattern is qualitatively similar to those obtained by other authors^{24,25} and is shown here primarily for illustrative purposes.

Wavefronts spread essentially according to Huygen's principle up to small curvature corrections to the conduction velocity.²⁴ Consequently, if there were no fiber rotation, isochrone lines (lines of constant arrival times of the wavefront) on the epicardium would appear as simple spreading ellipses. With fiber rotation, however, the isochrone lines twist in time and change shape, as shown in Fig. 2. One way to understand qualitatively the origin of this twist is to imagine how the excitation wavefront would look like if the various planes inbetween the endocardium and epicardium were not electrically coupled, except along a transmural cable that passes through the point of stimulation. In this case, the isochrone surface would consist of stacked up ellipses that rotate with depth, each ellipse having a major axis of length $c_{\parallel}(t - z/c_{\perp 2})$ aligned with the local fiber axis, and a minor axis of length $c_{\perp 1}(t - z/c_{\perp 2})$, where z is the depth measured from the epicardium in terms of Fig. 1, t (assumed $> S/c_{\perp 2}$) is the time after the stimulus is applied, and $z/c_{\perp 2}$ is the delay of stimulation with depth. In this case, the epicardial isochrones would still be simple ellipses. In contrast, when the planes are electrically coupled, the excitation can spread back to the epicardium from deeper layers. This vertical spread effectively averages the elliptical isochrones over depth and tends to twist the isochrones at the surface and modify their overall shape. At least qualitatively, these effects are simple geometrical consequences of Huygen's principle in the presence of rotational anisotropy.

C. Rotational anisotropy, vortex twist, and VF

1. Simulation and experiment

On the theoretical side, computational limitations have made it difficult to carry out detailed quantitative studies of the effect of rotational anisotropy on reentry in continuous myocardium. Numerical studies in coarsely discretized myocardium have however been carried out. Panfilov and Keener²⁸ have interestingly observed that rotational anisotropy could destabilize reentry for a modified FitzHugh–Nagumo model. However, they used a grid spacing ~ 1 mm to mimic anisotropic refractoriness that induces a large jump in angle between layers and makes it hard to relate their results to real myocardium. Moreover, so far, the underlying spatiotemporal dynamics of filament motion and twist has not been studied in the presence of rotational anisotropy in either discrete or continuous media.

On the experimental side, sustained VF is generally not supported by small hearts.^{29–33} Zipes *et al.*³⁰ have shown that canine RV does not support VF but the thicker LV does. Furthermore, Kavanagh *et al.*³¹ have observed VF in the LV only above a critical thickness. The main conclusion of these experiments, emphasized by Winfree^{32,33} is that hearts below a critical (electrically active) muscle thickness do not fibrillate, but support instead stable forms of tachycardia that one

can associate with a single spiral wave. The present data, however, do not suffice to conclude whether it is the thickness of ventricular muscle, rotational anisotropy, or a combination of both, which is the main cause of VF as reviewed recently by Winfree.^{32,33}

2. Vortex twist

Attempting to understand the effect of rotational anisotropy on reentry and VF naturally leads one to ask questions about its effect on the twist of transmural vortex lines of phase singularity (or filaments) that end normal to the epicardium and endocardium. A constant twist along a straight infinite line can be pictured by imagining drawing spiral waves in closely spaced planes perpendicular to this line and rotating slightly each spiral by a constant angle as one moves up from one plane to the next. In this case the twist is simply $W = 2\pi/d$ where d is the distance along the vortex line over which the spiral wave has made one complete rotation. In more general situations, vortex lines need not be straight and twist need not be uniformly distributed along them. One can then define a local twist³⁴ that measures the rate of rotation of the wavefront in successive planes that are locally perpendicular to this line as discussed in Sec. VI. For the idealized presentation of Fig. 1, the local twist of a transmural vortex line must vanish at the epicardium and the endocardium because of the mirror symmetry at these boundaries. So twist in myocardium cannot be constant along vortex lines and is largest intramurally.

Twist has been studied primarily in isotropic excitable media and in the simpler regime of nonmeandering spiral waves, i.e., spiral waves that rotate rigidly around a small circular core (elliptical in cardiac tissue) as discussed more at length in Sec. V. It has been investigated both analytically^{35–39} and numerically (Ref. 40 with earlier references therein) in two-variable reaction diffusion models, as well as experimentally in the Belousov–Zhabotinskii (BZ) reaction.^{41,42} Twist has been traditionally induced by imposing a gradient of parameter parallel to the filament, which makes one end of the filament spin faster than the other, or by imposing boundary conditions that have a similar effect. Several findings of these studies have been argued to be potentially relevant for myocardium:⁴³

- (i) Twist has been observed experimentally in BZ⁴¹ to relax diffusively in agreement with existing analyses of twist perturbations along a straight filament.^{36,37} This diffusive decay has been used as a basis to estimate³² the twist magnitude in myocardium (see below).
- (ii) Above some critical twist amplitude a morphological instability occurs that causes the filament shape to evolve from a straight line to a helix. The term *sproing* was first coined by Henze *et al.*⁴⁰ to describe this instability in a numerical study of twist in two-variable reaction diffusion models. The same instability was later observed experimentally by Mironov *et al.*⁴² in BZ. The critical twist was found to be about 2/3 of one rotation per wavelength in both simulation⁴⁰ of the Oregonator model (two-variable

caricature of the BZ reaction) and experiment,⁴² or $W_c \approx 4\pi/3\lambda$. Slightly different magnitudes of W_c were found for other forms of FitzHugh–Nagumo kinetics.⁴⁰

- (iii) The spin rate of scroll waves increases with twist.^{35,36} Independently of this increase, and for purely geometrical reasons,^{40,43} twist also packs wavefronts closer together, thereby decreasing the excitable gap. Thus a sufficiently large twist can cause the excitable gap to fall below a minimum value at which stable plane wave propagation fails and localized wave breaks are created. This type of “patchy failure” can in turn induce a transition to a wave turbulent state that has been observed experimentally in BZ under strong gradient condition.⁴¹

One can attempt to examine the relevance of twist in myocardium by estimating its average amplitude. Some of these estimates have been carried out by Winfree in Refs. 43, 32. In general, twist can be induced either by the transmural gradient of refractory period between the endocardium and epicardium (the refractory period being about 10% shorter on the epicardium than on the endocardium) or by rotational anisotropy. Although we focus more on the latter mechanism in this paper, it is worthwhile to estimate the amplitudes resulting from each mechanism separately.

Twist caused by a gradient of refractory period can be estimated³² by calculating the rate of twist buildup k_b and the time t_d it takes for twist to decay. It then follows that the twist amplitude $\bar{W} \sim k_b t_d$. Assuming purely diffusive untwisting (e.g., Refs. 36, 41, 32),

$$\partial_t W = D_{\perp 2} \partial_z^2 W, \quad (1)$$

subject to the two boundary conditions $W(0) = W(S) = 0$ imposed by symmetry at the two bounding surfaces. Substituting a simple Fourier sine series $W(z, t) = \sum_n W_n(t) \sin(n\pi z/S)$ into this equation yields $W_n(t) = W_n(0) \exp(-t/t_n)$ with $t_n = S^2/(n^2 \pi^2 D_{\perp 2})$. The slowest, and hence most meaningful, relaxation time corresponds to $n=1$, which yields at once the expression $t_d \approx S^2/(\pi^2 D_{\perp 2})$ used previously by Winfree to estimate twist in myocardium.³² Let us now denote by $\Delta\omega$ the difference of angular frequencies of rotation of spiral waves on the epicardium and endocardium, and by $\bar{\omega}$ the average of these two frequencies. The rate of twist buildup, or winding of the filament, is then simply $k_b = \Delta\omega/S$, which yields $\bar{W} \sim k_b t_d \sim S \Delta\omega/(\pi^2 D_{\perp 2})$. In comparison, the critical twist necessary for sproing is $W_c \approx 2\pi f_c/\lambda$, where $\lambda \approx 2\pi c_{\perp 2}/\bar{\omega}$ is the transmural wavelength and f_c is some, as yet unspecified, critical fraction of one complete rotation necessary for sproing. Equating the estimates of W_c and \bar{W} , we get a critical thickness for sproing equal to

$$S_c \approx \frac{f_c \pi^2 D_{\perp 2} \bar{\omega}}{c_{\perp 2} \Delta\omega}. \quad (2)$$

For $D_{\perp 2}$ in the range of 1/9 to 1/5 cm²/s, $c_{\perp 2} \approx 15$ cm/s, $\Delta\omega/\bar{\omega} \approx 0.1$, and $f_c \approx 2/3$, assuming that the BZ threshold for

sproing applies to myocardium, we obtain that S_c is between 1/2 and 1 cm and that twist builds up over about 1 s for 1 cm. So the RV is stable by that argument and the LV is unstable against sproing. [Winfree concluded in Ref. 32 that the LV should be stable by the present estimation. This is because of a calculator error (Ref. 44) equivalent to substituting $9 \text{ cm}^2/\text{s}$, instead of $1/9 \text{ cm}^2/\text{s}$, for $D_{\perp 2}$ in Eq. (2), which leads to an estimate of t_d two orders of magnitude smaller than here. We shall argue later in this paper that, even corrected, this estimate may not be relevant for continuous myocardium, such that this footnote is more of historical interest to avoid confusion.]

Let us now turn to the relation between rotational anisotropy and twist. With zero electrical coupling between layers one can construct a scroll wave consisting of stacked spiral waves that are simply dilated along the fiber axis and contracted perpendicular to it. Such a scroll filament has zero twist. However, it is easy to work out that such a state is destroyed by a finite coupling since it is not translationally invariant along the transmural axis. Although this does not prove that there does not exist some other scroll wave state that also has zero twist with a finite coupling, we would expect generic states to have a finite twist as a result of interlayer diffusion. However, there is presently no reliable theory, even approximate, to estimate what this amplitude may be. One crude way to estimate twist, but not correct as we shall see later, is to assume that the phase change across the ventricle is roughly equal to the total fiber rotation angle, and hence that $\bar{W} \approx \Delta \theta / S$. It leads to the conclusion that the LV is stable against sproing (but not necessarily propagation failure) for $\theta_z \approx 120^\circ/\text{cm}$.

Another argument that can be made is that rotational anisotropy should not continuously wind the filament in the same way as a gradient of refractoriness. Any finite amount of twist, if present, should build up on a time scale comparable to the average period $\bar{T} = 2\pi/\bar{\omega}$, at least for nonmeandering spiral waves. This implies that rotational anisotropy should have a negligible effect when t_d is shorter than \bar{T} , or equivalently $S < S_{\min} \sim \pi(D_{\perp 2}\bar{T})^{1/2}$. This yields S_{\min} in the range of 3–5 mm for $D_{\perp 2}$ between 1/9 and 1/5 cm^2/s and $\bar{T} = 100 \text{ ms}$. So the RV is just stable by this estimate.

3. Open questions

At present, it is unclear that the above crude estimates are correct. First, as discussed in more detail in Sec. V, spiral waves in ionic models of ventricular action potential, and in experiment, exhibit highly nonlinear meander patterns under normal excitability condition. One therefore needs to understand twist dynamics in such a regime, which is not the one described by current analytical theories, or studied so far in most simulations. Second, nothing is known about twist in the presence of rotational anisotropy.

In view of the foregoing review, some of the most relevant open questions are: (i) How is twist built-up and relaxed in space and time? (ii) How large is the twist induced by rotational anisotropy as a function of wall thickness (S) and fiber rotation rate (θ_z)? (iii) Can twist destabilize filaments? (iv) Lastly, can such an instability produce the wave

turbulence characteristic of VF above some critical muscle thickness and/or fiber rotation rate? As we shall see, the numerical results of Sec. VII require us to critically reexamine the above estimates that turn out not to be applicable. They show that rotational anisotropy induces a twist that is neither constant in time nor distributed along the filament as a half-sine wave, as assumed in all the above diffusive estimates. Instead, during one rotation, there are intermittent periods where the filament is nearly straight and untwisted, and shorter periods where the filament is folded and highly twisted along a small section. New estimates will be proposed to interpret these results.

We conclude this section by mentioning a related open issue. Namely, is VF necessarily a 3D phenomenon, which the reader may be led to believe from the present emphasis on rotational anisotropy, or can it be a purely 2D phenomenon? Atrial fibrillation left aside, the classic sheet preparation of Davidenko *et al.*⁷ does not support wave turbulence,⁷ but a single drifting spiral wave. This fact alone, however, does not prove that VF is not intrinsically a 2D phenomenon for two reasons. First, this preparation alters the electrophysiology (in particular the excitability) in a way that may tend to suppress wave instabilities. Second, Gray *et al.*^{45,46} have provided experimental and theoretical evidence that even a single spiral wave drifting across the heart surface is sufficient to produce a VF-like ECG, although apparently not in agreement with other experiments that seem to converge to the more traditional view that several rotors are involved.^{9,47} In a recent experiment, Garfinkel *et al.*¹⁰ reproduced the sheet preparation of Davidenko *et al.* with a 1 to 2 mm thick and 25 mm in length and width slice of right ventricular epicardium. They further added a drug agent that shortens the action potential duration (APD) by 30%–50%, and hence the spiral wavelength $\lambda \sim \text{conduction velocity} \times \text{APD}$ thereby effectively making the tissue larger. They observed a multiple-rotor VF-like state with the drug agent, demonstrating that such a state is at least experimentally possible in a quasi-2D preparation with altered electrophysiology, but not without.

On the theoretical side, numerous simulations of complex^{48–51} and simplified ionic models^{52–54,10} have also demonstrated that wavefront fragmentation leading to either transient or sustained complex wave behavior is, in principle, possible in 2D. However, none of the theoretical mechanisms that have been proposed to explain this fragmentation, including stationary repolarization fronts^{49,50} and electrical alternans,^{53,54} both based on an action potential duration restitution curve with a slope significantly larger than one, or a shortened relative refractory period,⁵² have been tested experimentally. So the issue of whether VF is essentially a 2 or 3D phenomenon is still largely open both experimentally and theoretically. Future progress on this issue will rely on a better understanding of how drug agents alter the electrophysiology of sheet preparations, and hence the stability of rotors, and the development of better tools to characterize spatiotemporal organization during VF in whole hearts (see for example the article by Bayly *et al.* in this issue).⁴⁷ We return to this issue at the end of Sec. V where we examine experimentally measured restitution curves and those pro-

duced by ionic models of ventricular action potential. Our conclusion is that the most believable curves are not steep enough to produce VF in 2D.

III. SIMULATING WAVE PROPAGATION IN CONTINUOUS MYOCARDIUM

In this section we present an algorithm for solving the monodomain cable equations in a 3D parallelepipedal slab of continuous tissue with rotational anisotropy.

A. Basic equations and boundary conditions

The basic equations have the form

$$\partial_t V = \nabla \cdot (\tilde{D} \nabla V) - I_{\text{ion}}(V; \mathbf{y}) / C_m, \quad (3)$$

$$\partial_t \mathbf{y} = \mathbf{g}(V; \mathbf{y}), \quad (4)$$

where V is the membrane potential, I_{ion} is the total current flowing through the membrane, C_m is the membrane capacitance, \mathbf{y} is a vector (y_1, y_2, \dots) of gate variables that prescribes the dynamics of the various currents that make up I_{ion} , ∇V denotes the gradient operator with components $(\partial_x V, \partial_y V, \partial_z V)$, and

$$\tilde{D} \equiv \frac{\tilde{\sigma}}{S_o C_m} = \begin{pmatrix} D_{11} & D_{12} & 0 \\ D_{21} & D_{22} & 0 \\ 0 & 0 & D_{\perp 2} \end{pmatrix}, \quad (5)$$

where $\tilde{\sigma}$ is the conductivity tensor and S_o is the cell surface to volume ratio. The matrix elements are defined by

$$D_{11} = D_{\parallel} \cos^2 \theta(z) + D_{\perp 1} \sin^2 \theta(z), \quad (6)$$

$$D_{22} = D_{\parallel} \sin^2 \theta(z) + D_{\perp 1} \cos^2 \theta(z), \quad (7)$$

$$D_{12} = D_{21} = (D_{\parallel} - D_{\perp 1}) \cos \theta(z) \sin \theta(z), \quad (8)$$

where the diffusivities are for propagation parallel to the fiber axis (D_{\parallel}), perpendicular to this axis in each plane, ($D_{\perp 1}$), and transmurally ($D_{\perp 2}$), and

$$\theta(z) = -\Delta \theta / 2 + z(\Delta \theta / S) \quad 0 \leq z \leq S \quad (9)$$

measures the angle between the fiber and the y-axis in each plane. Equation (9) is equivalent to assuming that the fiber axis rotates continuously between the epicardium ($z=0$) and endocardium ($z=S$) as depicted in Fig. 1.

We restrict our attention to an electrically insulated piece of tissue and therefore impose that there is no net current flow normal to the surfaces bounding the tissue. This yields the Neumann boundary conditions

$$\hat{n} \cdot (\tilde{D} \nabla V) = 0, \quad (10)$$

where \hat{n} is the normal unit vector to each of the six bounding surfaces, or, equivalently,

$$\partial_z V = 0 \quad (\text{at } z=0 \text{ and } z=S), \quad (11)$$

$$D_{11} \partial_x V + D_{12} \partial_y V = 0 \quad (\text{at } x=0 \text{ and } x=L_x), \quad (12)$$

$$D_{21} \partial_x V + D_{22} \partial_y V = 0 \quad (\text{at } y=0 \text{ and } y=L_y). \quad (13)$$

We have not explored more realistic types of boundary conditions where the tissue is in contact with a bath, or included the effect of the endocardial Purkinje network, which could

be important.⁵⁵ Our prime motivation has been to first understand vortex dynamics with the simplest possible set of boundary conditions that approximates bulk ventricular tissue without the Purkinje network. Understanding the effects of more realistic boundary conditions and this network remains an interesting task for the future.

B. Algorithm

1. Spatial discretization

We discretize the PDE by defining V_{α}^n where the three-dimensional index $\alpha \equiv (i, j, k)$ denotes the position on the lattice, or $\mathbf{r} = i\Delta x \mathbf{x} + j\Delta y \mathbf{y} + k\Delta z \mathbf{z}$, where $\Delta x = \Delta y = \Delta$, and Δz are lattice spacings, and n measures the time $t \equiv n\Delta t$. The partial derivatives $\partial_x^2 V$, $\partial_y^2 V$, $\partial_z^2 V$, and $\partial_{xy}^2 V$ are approximated by standard centered difference formulae $\Delta^{-2} \delta_x^2 V_{\alpha}^n$, $\Delta^{-2} \delta_y^2 V_{\alpha}^n$, $\Delta z^{-2} \delta_z^2 V_{\alpha}^n$, and $\Delta^{-2} \delta_{xy}^2 V_{\alpha}^n$, respectively, where

$$\delta_x^2 V_{\alpha}^n \equiv V_{i+1,j,k}^n + V_{i-1,j,k}^n - 2V_{i,j,k}^n, \quad (14)$$

$$\delta_y^2 V_{\alpha}^n \equiv V_{i,j+1,k}^n + V_{i,j-1,k}^n - 2V_{i,j,k}^n, \quad (15)$$

$$\delta_z^2 V_{\alpha}^n \equiv V_{i,j,k+1}^n + V_{i,j,k-1}^n - 2V_{i,j,k}^n, \quad (16)$$

$$\delta_{xy}^2 V_{\alpha}^n \equiv \frac{1}{4} [V_{i+1,j+1,k}^n - V_{i+1,j-1,k}^n - V_{i-1,j+1,k}^n + V_{i-1,j-1,k}^n]. \quad (17)$$

2. Time stepping scheme

In cardiac muscle, the elements of the diffusion tensor \tilde{D} are of the order of $1 \text{ cm}^2/\text{s}$. Furthermore, resolving the continuum limit of the cable equations typically requires choosing a grid spacing $\Delta \approx 200\text{--}300 \mu\text{m}$ because of the narrowness of the wavefront (\sim conduction velocity $\times 1 \text{ ms}$) for normal membrane excitability. This restricts Δt to a few hundredth of a ms because of the numerical stability constraints associated with explicit schemes (see below). The algorithm we use is *unconditionally stable* for isotropic propagation, with no restriction on Δt other than accuracy. For anisotropic propagation with fiber rotation, it is subject to a much less stringent constraint on Δt than Euler. It therefore permits use of simultaneously a small Δ , needed to resolve the continuum limit of the cable equations, and a value Δt in the range of a couple tenths of a ms that renders the simulations considerably more efficient.

The only nontrivial part of the algorithm is based on using the method of operator splitting to step semi-implicitly the diagonal part of the spatial operator $\sim D_{11} \delta_x^2 V + D_{22} \delta_y^2 V + D_{\perp 2} \delta_z^2 V$. The cross term $\sim \delta_{xy}^2 V$ is then simply treated explicitly and $I_{\text{ion}}(V; \mathbf{y})$ is treated semi-implicitly by linearizing I_{ion} about the value of V at the previous time step. For clarity of exposition, it is therefore best to describe the algorithm for the case of purely isotropic diffusion with $D_{\parallel} = D_{\perp 1} = D_{\perp 2} \equiv D$ and $I_{\text{ion}} = 0$. The straightforward extension to anisotropic propagation with $I_{\text{ion}} \neq 0$ is described in Appendix A.

Let us first recall the Euler scheme defined for isotropic propagation by

$$V_{\alpha}^{n+1} = V_{\alpha}^n + \beta (\delta_x^2 V_{\alpha}^n + \delta_y^2 V_{\alpha}^n + \delta_z^2 V_{\alpha}^n), \quad (18)$$

where $\beta \equiv D\Delta t/\Delta^2$ and we have let here $\Delta z = \Delta$. A standard von Neumann linear stability analysis⁵⁶ of this scheme leads to the well-known result that it is only stable if $\beta < 1/(2d)$ in d dimensions, and therefore if $\beta < 1/6$ in 3D.

We follow a scheme that utilizes operator splitting.⁵⁶ We first split the 3D Laplacian operator as the sum of two operators: $O_1 \equiv \delta_x^2 + \delta_y^2$, corresponding to the 2D Laplacian in the x - y plane, and, $O_2 \equiv \delta_z^2$, corresponding to diffusion along z . We are then free to choose how to time step each operator separately. We choose here to step O_1 using a two-dimensional alternating direction implicit (ADI) scheme and O_2 using a one-dimensional implicit scheme. This choice can easily be shown by a von Neumann stability analysis to yield an unconditionally stable scheme. Let us denote by V_α^S the result of the first split step, $V_\alpha^n \rightarrow V_\alpha^S$, with O_1 . The result of the second split step, $V_\alpha^S \rightarrow V_\alpha^{n+1}$, with O_2 is then just V_α^{n+1} . This yields the scheme defined by

$$\left. \begin{aligned} V_\alpha^S &= V_\alpha^n + \beta(\delta_x^2 V_\alpha^n + \delta_y^2 V_\alpha^n) \\ V_\alpha^{n+1} &= V_\alpha^S + \frac{\beta}{2}(\delta_z^2 V_\alpha^{n+1} + \delta_z^2 V_\alpha^S) \end{aligned} \right\} \quad n \text{ even}, \quad (19)$$

$$\left. \begin{aligned} V_\alpha^S &= V_\alpha^n + \beta(\delta_x^2 V_\alpha^n + \delta_y^2 V_\alpha^n) \\ V_\alpha^{n+1} &= V_\alpha^S + \frac{\beta}{2}(\delta_z^2 V_\alpha^{n+1} + \delta_z^2 V_\alpha^S) \end{aligned} \right\} \quad n \text{ odd}. \quad (20)$$

The n even and odd steps are identical except for the interchange of x and y that corresponds to alternatively stepping x and y implicitly every two time steps. The important point here is that the number of floating point operations for one time step is, like for Euler, proportional to the total number of grid points $N_x N_y N_z$ on the lattice (where $L_x = N_x \Delta$, $L_y = N_y \Delta$, $L_z = N_z \Delta$). Each iteration only requires to solve a series of linear systems of equations of the form $\mathcal{L}V = R$ where \mathcal{L} is a tridiagonal matrix, V is an unknown one-dimensional vector, and R is some known right-hand side vector. This can be efficiently done in order N operations where N is the length of vector V . More specifically, Eq. (19) implies that, for n even, calculating V_α^S requires solving $N_y N_z$ independent tridiagonal systems for each pair of indices (j, k) . Each system has for unknown the one-dimensional vector $V_{i,j,k}^S$ of length N_x indexed by $i \in [1, N_x]$. Calculating V_α^{n+1} at the second split step then requires to solve $N_x N_y$ independent tridiagonal systems for the unknown vectors $V_{i,j,k}^{n+1}$ of length N_z indexed by $k \in [1, N_z]$. By symmetry, for n odd [Eq. (20)], the first split step requires to solve $N_x N_z$ separate tridiagonal systems with unknown vectors of length N_y indexed by $j \in [1, N_y]$ in order to calculate V_α^S . The second split step is the same as for n even.

IV. SIMPLIFIED THREE-CURRENT IONIC MODEL OF VENTRICULAR ACTION POTENTIAL WITH RESTITUTION

A. Motivation

Ionic models that describe ventricular action potential^{11–15} have become increasingly more complex, and hopefully more realistic as a result. These models characterize I_{ion} in Eq. (3) by gathering various membrane currents measured in classic voltage-clamp or patch-clamp experi-

ments. Although current computing platforms allow simulating the 20 year old version¹² of these models in 2D for a few rotation periods,^{49–51} they do not allow one to carry out extensive 3D simulations. Moreover, the overwhelming complexity of the latest models^{14,15} makes it difficult to isolate a subset of essential parameters. Lastly, and most importantly in our view, ionic models may not faithfully reproduce the restitution properties (defined below) of action potential in myocardium despite their complexity.

One traditional escape from this complexity has been to use simplified models of excitable media as “caricatures” of myocardium. The best known example is the FitzHugh–Nagumo (FN) model,⁵⁷ described in its simplest form by the equations

$$\partial_t u = \nabla \cdot (\tilde{D} \nabla u) + 3u - u^3 - v, \quad (21)$$

$$\partial_t v = \epsilon(u - \delta), \quad (22)$$

where u is a dimensionless measure of the membrane potential, v is some effective membrane conductance, ϵ is a small parameter that measures the abruptness of excitation, relative to the pulse duration, and δ is a parameter that measures the excitability of the membrane, i.e., the amplitude of the stimulus necessary to cause an excitation.

The FN model has been (and remains) extremely useful to gain basic insight into the wave behavior of generic excitable media, and in particular to understand how this wave behavior depends on a reduced set of parameters such as ϵ and δ (see Ref. 58 with references therein). However, it has become recognized that this model does not reproduce, even qualitatively, certain important properties of ventricular action potential.^{59,60,54} As a result, modified forms of the FN equations^{59,60,54} and truncated versions of more complex models⁶¹ have been introduced. The so-called “Pushchino” FN kinetics⁵⁹ was introduced to shorten the relative refractory period, which is the period after repolarization during which the membrane recovers its resting properties. More recent simplified models have focused on incorporating restitution properties.^{60,54} However, so far, proper model validation by a close comparison of the two-dimensional reentry patterns produced by the simplified models and the more complex ones has not been systematically carried out.

B. Model

Here we describe a model that retains the minimal ionic complexity necessary to reproduce *quantitatively* the restitution curves that describe how the pulse duration and its propagation velocity depend on the time interval after repolarization during which the membrane recovers its resting properties. We shall show in Sec. V that once these two curves are correctly reproduced for a given electrophysiological model, the two-dimensional spiral wave behavior of this model is also reasonably well-reproduced quantitatively. In addition, this modeling approach allows making contact directly with real tissue by fitting experimentally measured restitution curves.

1. Restitution of action potential duration and conduction velocity

The action potential duration restitution curve,^{17,18} referred to hereafter as APD restitution, relates the APD at a given point in the tissue with the previous diastolic interval DI at the same point. This DI, or recovery time, measures the time between successive repolarization and depolarization of the membrane, measured at the same threshold membrane potential as the APD (typically $\approx 80\% - 95\%$ repolarization of V). The membrane *recovers* its resting properties during this interval until the next excitation. Typically, a DI that is sufficiently long for the membrane to have fully recovered will be followed by a long APD that is independent of the DI. In contrast, a short DI that only allows partial recovery will be followed by a short APD. Therefore the APD restitution curve incorporates in a single curve all the ionic complexity underlying the relationship between the pulse duration and the partially recovered state of the tissue. The importance of APD restitution in cardiac dynamics has been emphasized in numerous studies. A sufficiently steep restitution curve can lead to a period doubling instability of the APD of a single cell under rapid pacing,^{62–64} to related quasi-periodic oscillations of APD during circular motion of a pulse in a ring of tissue,^{65–69} as well as to slow repolarization fronts^{49,50} and wavelength oscillations⁵⁴ that can cause wavebreaks in a 2D tissue.

Another fundamental property of waves in excitable media is the so-called dispersion curve that traditionally relates the steady-state velocity of a plane wave train with its period (see for example Ref. 70). This curve can also be defined to relate the *instantaneous* conduction velocity (CV) of an excitation wavefront to the previous DI at the point where the velocity is measured. The CV generally depends on the orientation of the wavefront with respect to the fiber axis. However in a continuous medium we can arbitrarily choose to define this curve for propagation parallel to the fiber axis. Propagation in the two principal directions perpendicular to the fiber axis is then characterized by the same curve scaled down by a factor of $(D_{\perp,2}/D_{\parallel})^{1/2}$. Purely as a matter of choice, we prefer to refer hereafter to this curve as CV restitution rather than dispersion. Dispersion is traditionally used in the cardiology literature to describe spatial variations of refractoriness, which can lead to confusion. More importantly, this curve is directly analogous to the APD restitution curve from a physiological standpoint. It describes how the CV is recovered as the tissue returns to its resting properties. Generally conduction is slower in partially recovered tissue such that the CV decreases with decreasing DI, down to some minimum interval DI_{\min} where propagation fails. Finally, it is simple to show that once a given CV restitution curve of a more complex model is correctly reproduced by the simplified model, the Eikonal equation²⁴ that describes the effect of wavefront curvature on the spread of excitation is also automatically reproduced by choosing the same diffusivity tensor \tilde{D} in both models.

We concentrate on the APD and CV restitution curves because they are the ones that dictate the dynamics of the depolarization wavefront and repolarization waveback, and the interaction between these two fronts. They are therefore

more fundamental quantities for modeling wave dynamics than the shape of the action potential.

2. Ionic currents and basic equations

To capture these properties, I_{ion} is written as the sum of three currents:

$$I_{\text{ion}} = I_{\text{fi}}(V;v) + I_{\text{so}}(V) + I_{\text{si}}(V;w), \quad (23)$$

where (i) I_{fi} is a fast inward current that is responsible for depolarization of the membrane and only depends on one inactivation–reactivation gate v , i.e., which is responsible for inactivation of this current after depolarization and its reactivation after repolarization. The role of this gate is directly analogous to that of the product $h \times j$ of the gates h and j of the sodium current in the Beeler-Reuter¹² and Luo-Rudy¹⁵ models. (ii) I_{so} is a slow outward current $I_{\text{so}}(V)$ that is analogous to the time-independent potassium current in these models and is responsible for repolarization of the membrane. (iii) I_{si} is a slow inward current, analogous to the calcium current, that balances I_{so} during the plateau phase of the action potential and only depends on one gate variable w , responsible for inactivation and reactivation of this current, which is analogous to the gate f of the calcium current.^{12,15} Even though in a classic physiological picture of membrane dynamics, I_{fi} , I_{so} , and I_{si} correspond to the Na, K, and Ca currents, respectively, this correspondence is an oversimplification since the known membrane dynamics is far more complex¹⁵ than caricatured by these three currents. However, the goal here is not to reproduce details of individual ionic currents, but to retain the minimal ionic complexity that underlies the membrane recovery processes that give rise to generic restitution curves. For this reason, we prefer to refer to these currents as fast and slow inward, and slow outward, rather than Na, Ca, and K, as a reminder that they do not represent quantitatively measured currents, but only their activation, inactivation, and reactivation dynamics necessary to reproduce quantitatively restitution properties.

In this respect, the present model overcomes several limitations of a model introduced previously by one of us.⁵⁴ This model exploited a modified FN-like nullcline structure and kinetics in order to attempt to reproduce arbitrary restitution curves.⁵⁴ Although arbitrary in shape, these curves were constrained in this model to have a minimum APD and CV that both become vanishingly small in the limit $\epsilon \ll 1$ representative of normal myocardium. As shown below, experimentally measured curves, as well as those produced by ionic models, terminate at a finite APD and velocity even when the excitation is very abrupt. The present more physiologically based model is not subject to these restrictions that apply to two-variable models with a nullcline structure. The minimum conduction velocity along the CV restitution, below which propagation failure occurs, is now controlled by the rate of inactivation of the sodium current, independently of the smallness of the ratio ϵ of the time scale $\tau_d \equiv C_m / \bar{g}_{\text{fi}}$ to depolarize the membrane and the APD. Furthermore, the minimum APD can be controlled by the slow outward and inward currents also independently of ϵ .

It is convenient to write down the equations of the model by defining the dimensionless membrane potential u

$\equiv (V - V_o)/(V_{fi} - V_o)$ that varies from 0 to 1, where V_o is the resting membrane potential, and V_{fi} is the Nernst potential of the fast inward current. It is also convenient to define the scaled currents $J_{fi} = I_{fi}/(C_m(V_{fi} - V_o))$ (same for J_{so} and J_{si}) that have units of inverse time. The equations of the model then become

$$\partial_t u = \nabla \cdot (\tilde{D} \nabla u) - J_{fi}(u; v) - J_{so}(u) - J_{si}(u; w), \quad (24)$$

$$\partial_t v = \Theta(u_c - u)(1 - v)/\tau_v^-(u) - \Theta(u - u_c)v/\tau_v^+, \quad (25)$$

$$\partial_t w = \Theta(u_c - u)(1 - w)/\tau_w^- - \Theta(u - u_c)w/\tau_w^+, \quad (26)$$

where the three currents are given by

$$J_{fi}(u; v) = -\frac{v}{\tau_d} \Theta(u - u_c)(1 - u)(u - u_c), \quad (27)$$

$$J_{so}(u) = \frac{u}{\tau_o} \Theta(u_c - u) + \frac{1}{\tau_r} \Theta(u - u_c), \quad (28)$$

$$J_{si}(u; w) = -\frac{w}{2\tau_{si}} (1 + \tanh[k(u - u_c^{si})]). \quad (29)$$

$\Theta(x)$ is the standard Heaviside step function defined by $\Theta(x) = 1$ for $x \geq 0$ and $\Theta(x) = 0$ for $x < 0$, which reflects the fact that the gating functions $h_\infty(V)$, $m_\infty(V)$, $j_\infty(V)$, and $f_\infty(V)$, in the Beeler-Reuter¹² or Luo-Rudy-I¹⁴ models have been replaced by step functions. One exception is $d_\infty(V)$ that needs to be approximated by a smooth function (here the sigmoid form $(1 + \tanh[k(u - u_c^{si})])/2$) in order to produce a good fit of APD restitution curves. The APD is short if V does not reset after an excitation at a value sufficient to activate I_{si} . In contrast, the APD is long if I_{si} is activated. In order to accurately reproduce the CV restitution curve, we found it necessary to define the time constant that governs the reactivation of the fast inward current separately over two voltage ranges ($u_v < u < u_c$ and $u < u_v$) by defining the function

$$\tau_v^-(u) = \Theta(u - u_v)\tau_{v1}^- + \Theta(u_v - u)\tau_{v2}^-. \quad (30)$$

This splitting allows to vary independently the minimum diastolic interval (i.e., the excitable gap), controlled by τ_{v1}^- , and the steepness of this curve, controlled by τ_{v2}^- . We note that a good fit of the APD restitution curve could be obtained without introducing such a splitting for the reactivation process of the slow inward current.

C. Determination of model parameters

The values of V_o and V_{fi} only determine the range of membrane potential, i.e., the linear mapping that translates u into V . Therefore the nontrivial model parameters consists of the various time constants $\tau_d, \tau_o, \tau_r, \dots$, the threshold potentials u_c and u_c^{si} for activation of I_{fi} and I_{si} , respectively, the threshold potential u_v that enters in the definition of the $\tau_v^-(u)$, and the constant k . These parameters were chosen to fit the following restitution curves:

- (i) BR: Those obtained by $S1-S2$ stimuli of the Beeler-Reuter model with standard parameter values¹² in a 1D cable.
- (ii) MBR: Those obtained by $S1-S2$ stimuli of a modi-

fied version of the Beeler-Reuter model where the calcium kinetics is speeded up by dividing the functions $\tau_f(V)$ and $\tau_d(V)$ in Ref. 12 by a factor of 2 as in Refs. 49–51.

- (iii) MLR-I: Those obtained by $S1-S2$ stimuli of the Luo-Rudy-I model¹⁴ modified with the same calcium speed-up as MBR.
- (iv) GP: The experimental steady-state curves extracted by Girouard *et al.* (Fig. 5 in Ref. 19) from optical recordings of membrane potentials on the epicardial surface of the LV of a guinea pig (GP) during plane wave pacing at fixed cycle lengths. [The term steady state is commonly used to differentiate the curves measured by pacing at a fixed cycle length until constant APD and CV are obtained, from the restitution curves obtained by two successive stimuli ($S1$ and $S2$). In both the BR (MBR) and LR-I (MLR-I) models, there is little difference between these two curves except at small DI. In contrast, experimental pacing studies have shown that the $S1-S2$ and steady-state restitution curves differ significantly from each other even at longer DI.^{17,18} This is most likely due to longer memory effects⁷¹ that are not described by ionic models up to the LR-I model and are still poorly understood. The LR-II model¹⁵ incorporates other processes (sodium-potassium pump and calcium intake in the sarcoplasmic reticulum) that could potentially account for these observed memory effects, although this has not yet been demonstrated. In addition, no experimental studies have yet attempted to characterize memory effects that affect the conduction speed. We might be tempted to conjecture that such effects are present if we contrast the various CV restitution curves in Fig. 3 calculated by $S1-S2$ stimuli with the more gradually rising steady-state curve measured *in vivo*.¹⁹]

The BR model¹² was essentially the first detailed model of ventricular action potential following Noble's adaptation¹¹ of the classic Hodgkin-Huxley equations to the Purkinje fiber. The LR-I model¹⁴ is an improved version of the BR model with substantially faster, and more realistic, sodium kinetics. The calcium speed-up has been shown to be necessary to obtain stable rotors in 2D with BR kinetics.^{49–51} This necessity has been given different interpretations, both tied to APD restitution.^{50,69} Our simulations indicate that this speedup is not necessary to obtain stable rotors for the LR-I model which has a much less steep APD restitution curve. However, even in this case, it shifts down the (notoriously too long) maximum APD of this model in a more realistic range, ~ 200 ms, and is also useful for this reason. These models were chosen because they are presently accepted as useful, albeit not necessarily physiologically correct, reference models. The experimental curves¹⁹ have the advantage that they are directly measured *in vivo* and are thus subject to less uncertainties than the curves produced by any of the existing ionic models.

The restitution curves of the BR, MBR, and MLR-I models were calculated in a one-dimensional cable (plane

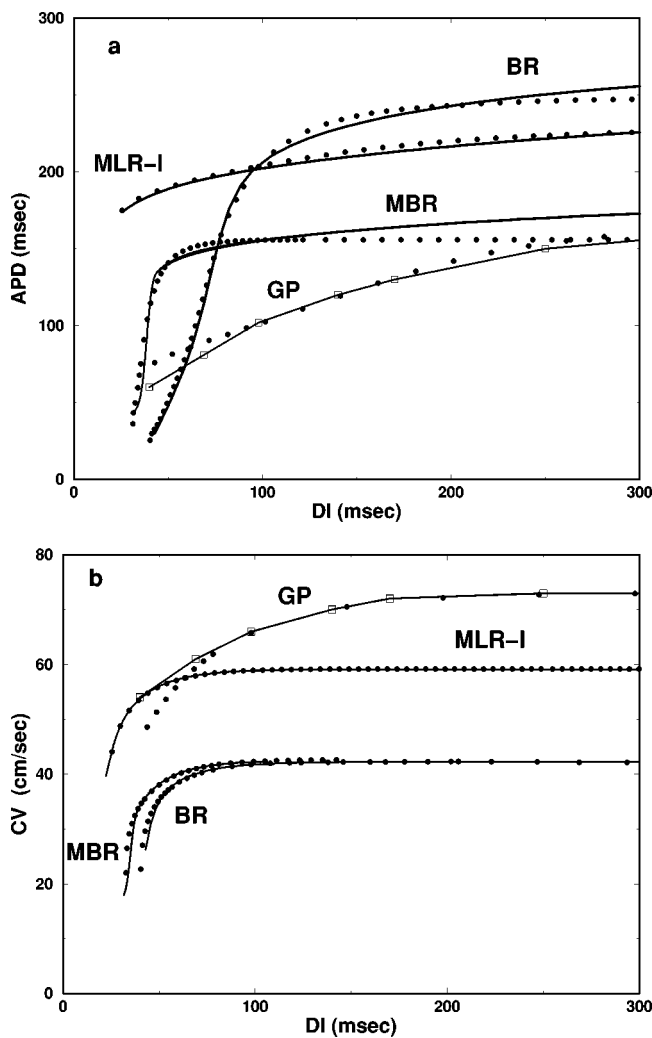


FIG. 3. Comparison of restitution curves of standard ionic models (solid lines) and those obtained from the simplified three-current model (filled circles) with the parameter sets of Table I: (a) action potential duration (APD) versus diastolic interval (DI); and (b) conduction velocity (CV) versus DI. Curves are obtained by two successive stimuli at one end of a 5 cm long cable with $D_{||} = 1 \text{ cm}^2/\text{s}$ and $V = -60 \text{ mV}$ as threshold to define the APD and DI in all models. Curves of standard ionic models include those of Beeler-Reuter (BR), modified Beeler-Reuter with speed-up calcium (MBR), and modified Luo-Rudy-I with speed-up calcium (MLR-I). Also fitted are the experimentally measured steady-state curves (open squares) of Ref. 19.

wave) geometry parallel to the fiber axis with $D_{||} = 1 \text{ cm}^2/\text{s}$. A first stimulus $S1$ was applied at one end of the cable to produce a first propagating action potential. A second stimulus $S2$ was then applied at the same end to initiate a second action potential in the tail of the first one. The restitution curves were then constructed by measuring the instantaneous speed of the second excitation wavefront and the APD as a function of the DI by varying the $S1$ – $S2$ interval. The results are shown in Fig. 3 together with the GP steady-state curves of Ref. 19.

The maximum conduction velocity is higher for MLR-I than either BR and MBR because of the faster sodium kinetics. In addition, the APD restitution curve of both BR and MBR terminates at a substantially shorter minimum APD ($\sim 40 \text{ ms}$) than the one of MLR-I (which terminate at

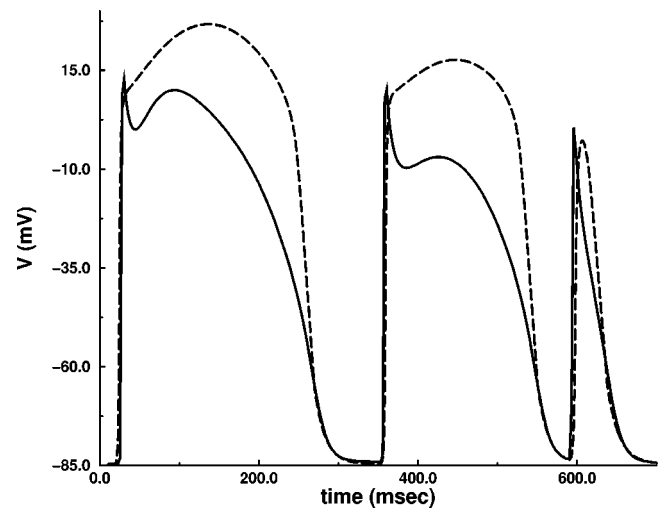


FIG. 4. Action potentials generated by three stimuli ($S1$ – $S2$ – $S3$) at one end of a 1D cable for the original BR model (solid line) and the simplified model (dashed line).

$\sim 160 \text{ ms}$). This difference may appear surprising at first since one would have naively expected restitution to be controlled by the slow membrane currents, which are quasi-identical in BR (MBR) and LR-I (MLR-I). However, a closer examination reveals that this difference is due to the slower Na kinetics in BR (MBR) that causes V to reset at a smaller peak value during excitation for small DI (Fig. 4), as compared to LR-I (MLR-I). As a result, the calcium current is not activated at short DI in BR (MBR), whereas it remains activated in LR-I (MLR-I). Restitution is built into our simplified model precisely in this way. So, contrary to naive expectation, APD restitution is generally controlled both by fast and slow membrane currents. We have insisted here on fitting the restitution curve obtained by $S1$ – $S2$ stimulation of a *propagating* pulse. The latter is only identical to the curve obtained by $S1$ – $S2$ stimulation of an isolated cell at long DI, but not at short DI where the APD is reduced. This is because cell coupling reduces the peak excitation value of V and hence the subsequent calcium influx that prologues the APD. One interesting conclusion is that increasing the sodium conductance increases the minimum APD and reduces the steepness of the APD restitution curve. So increasing the Na conductance of BR prevents spiral wave breakup.

The corresponding restitution curves calculated by $S1$ – $S2$ stimulation of the simplified three-current model [Eqs. (24)–(26)] in a 1D cable with the parameters of Table I are shown for comparison in Fig. 3. This comparison shows that the three-current model is able to reproduce these curves fairly accurately, as well as the pulse dynamics under repeated stimuli as illustrated in Fig. 4. Technical details of the fitting procedure that is used to determine the model parameters are not essential here and will be described elsewhere.⁷² Equation (24)–(26) and Table I provide the necessary information to independently reproduce all the computations of the present paper.

TABLE I. Parameters of the simplified three-current model obtained by fitting calculated restitution curves (see text) of the original Beeler-Reuter (BR) model, modified forms of the Beeler-Reuter (MBR) and Luo-Rudy-I (MLR-I) models with speedup calcium kinetics, and steady-state curves extracted from optical recordings on the LV epicardium of a Guinea pig (GP) during plane wave pacing parallel to the fiber at fixed cycle length (Ref. 19). Time is in unit of ms, $C_m = 1 \mu\text{F}/\text{cm}^2$, $\tau_d \equiv C_m / \bar{g}_{\text{fi}}$ with \bar{g}_{fi} in mmho/cm^2 , $V_o = -85 \text{ mV}$, $V_{\text{fi}} = +15 \text{ mV}$, and $k = 10$. Note that u_v does not need to be defined for MLR-I since $\tau_{v1} = \tau_{v2}$.

Parameter	BR	MBR	MLR-I	GP
\bar{g}_{fi}	4	4	5.8	8.7
τ_r	33	50	130	25
τ_{si}	30	45	127	22
τ_0	12.5	8.3	12.5	12.5
τ_v^+	3.33	3.33	10	10
τ_{v1}^-	1250	1000	18.2	333
τ_{v2}^+	19.6	19.2	18.2	40
τ_w^+	870	667	1020	1000
τ_w^-	41	11	80	65
u_c	0.13	0.13	0.13	0.13
u_v	0.04	0.055	-	0.025
u_c^{si}	0.85	0.85	0.85	0.85

V. MODEL VALIDATION

Two separate questions arise in validating ionic models. The first is whether simplified models, such as the one used here, semi-quantitatively reproduce the two-dimensional reentry pattern of more complex models, once the restitution curves have been fitted (a nontrivial test). The second question is whether the reentry patterns produced by any of the current models is representative of what is experimentally observed in myocardium.

The first question can be answered by directly comparing the reentry patterns of the simpler and more complex ionic model. This can be done, for example, for the BR and MBR models which have been simulated by Courtemanche and Winfree.⁴⁹ The precise meander trajectory generally depends on the way the wave tip (i.e., the end of the activation wavefront) is defined. However the basic features of this trajectory are independent of definition and can be meaningfully compared. We plot in Fig. 5 the wave tip trajectories (as defined in Sec. VI) obtained by simulation of the three-current model for the parameters (MBR, MLR-I, and GP) that produce stable re-entry in 2D. Contour plots of isopotential lines for MBR are shown in Fig. 6. The meander trajectories are made up of a succession of gently curved sections where the wavetip travels along arcs of conduction block parallel to the repolarizing waveback, and highly curved section (outward petals) at the end of these arcs where the wavefront pivots nearly in place around a short radius r . The morphology for MBR, including both the length of the arcs of block and the angle between successive arcs, is in relatively good agreement with the one simulated by Courtemanche and Winfree. Moreover, we find that reentry is unstable for the BR parameters. Wavebreaks occur that lead to the multiplication of vortices and a transient turbulent wave activity, also in good agreement with what these authors observe by full simulation of BR.⁴⁹ [There has been some confusion in the literature that is worth clarifying.

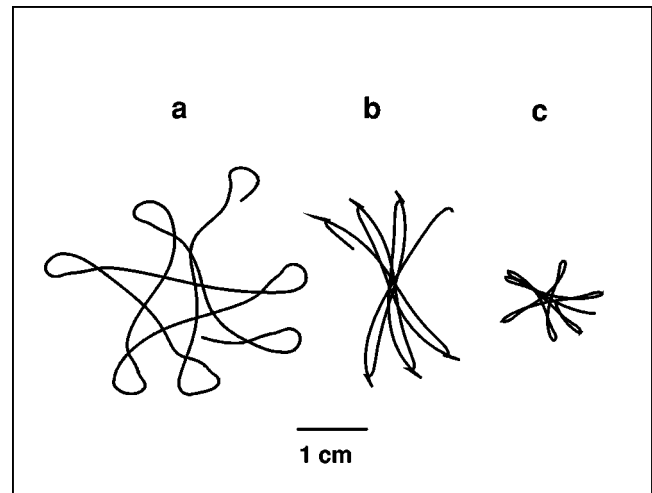


FIG. 5. Trajectories of the wavetip in a 2D isotropic tissue for the various fits of restitution curves that yield stable reentry: (a) MBR; (b) MLR-I; and (c) GP, with $D_{\parallel} = D_{\perp} = 1 \text{ cm}^2/\text{s}$, and $dx = 0.031 \text{ cm}$, $dt = 0.25 \text{ ms}$ for MBR, $dx = 0.0262 \text{ cm}$, $dt = 0.17 \text{ ms}$ for MLR-I, and $dx = 0.0215 \text{ cm}$, $dt = 0.115 \text{ ms}$ for GP. The wavetip position is calculated using Eq. (31) with $V_{\text{iso}} = -35 \text{ mV}$ for MBR, $V_{\text{iso}} = -25 \text{ mV}$ for MLR-I, and $V_{\text{iso}} = -45 \text{ mV}$ for GP.

While Courtemanche and Winfree⁴⁹ have reported that 2D reentry is unstable and transient in the BR model for standard parameter values, Krinsky *et al.*^{73–75} have reported that it is stable. The first rotation or so of reentry in BR proceeds along a line of block, as correctly described by Krinsky *et al.*, and may appear stable. Subsequent rotations, however, eventually lead to wavebreaks and transient reentry, as confirmed by our simulations.] Finally, a simulation of the MLR-I model⁷⁶ produces a linear core structure similar to Fig. 5(b).

Addressing the second question requires to summarize briefly what is known about spiral wave behavior in cardiac muscle. The trajectory of the wavetip usually depends on the excitability of the tissue. Excitability can be measured by the strength of the threshold stimulus necessary to cause an excitation. High (low) excitability is associated with a small (large) threshold stimulus and a fast (slow) propagation velocity. Normal myocardium is generally highly excitable, whereas ischemic tissue, i.e., tissue with reduced blood supply, can have a significantly lowered excitability and a shortened pulse duration.

Simulations to date in a variety of models (e.g., Refs. 2, 58, 73–75) have shown that, for low excitability, the wavetip simply rotates around a circular core region of resting tissue, whereas, for high excitability, the tip meanders along the aforementioned arcs of conduction blocks of Fig. 5. [Circular cores are elliptical in cardiac tissue because the propagation velocity is faster parallel than perpendicular to the fiber axis. In a 2D monodomain continuum, however, this anisotropy only amounts to a trivial contraction of the pattern perpendicular to the fiber axis that does not affect the dynamics. We therefore prefer to distinguish meander patterns in 2D in terms of their morphology in an isotropic medium. The highly anisotropic linear core structures are purely the product of the wave dynamics in an isotropic medium for normal

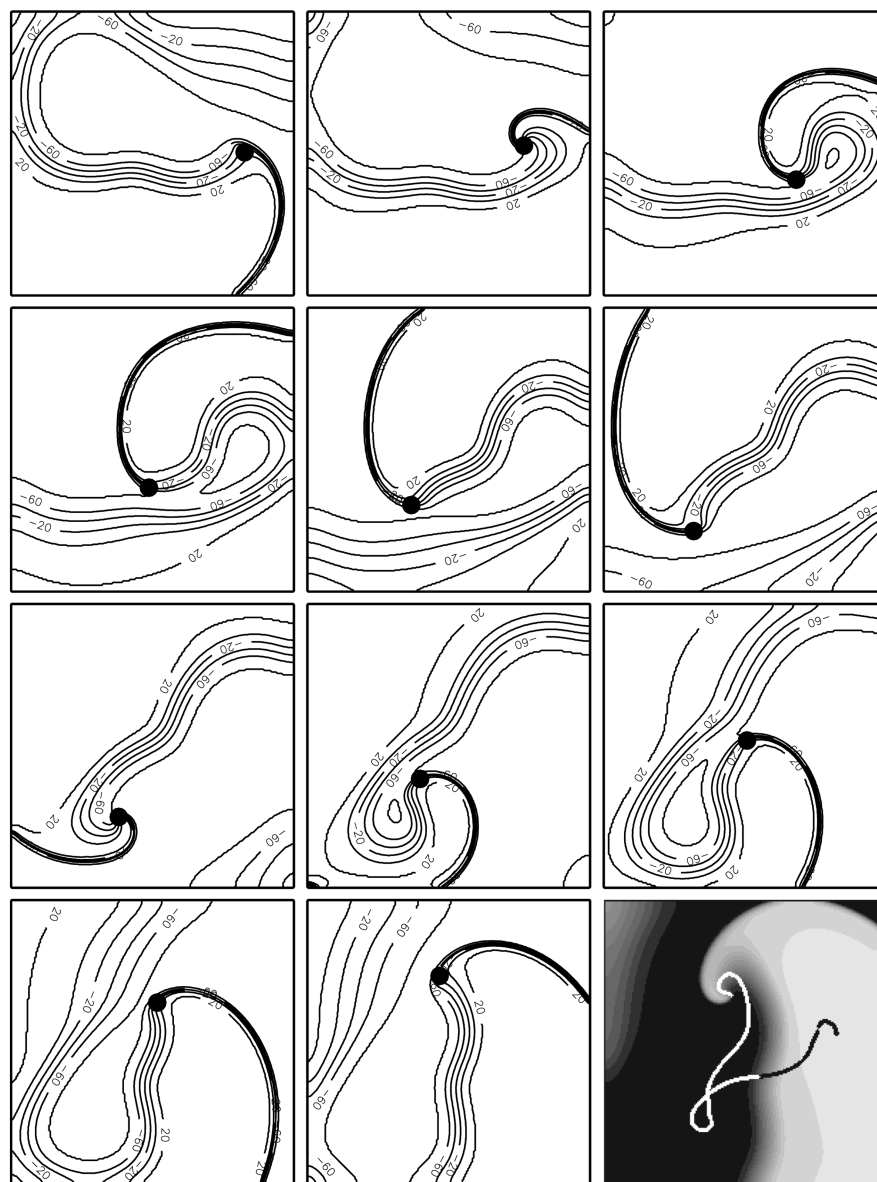


FIG. 6. Contour plots of V obtained by simulation of the three-current model with the modified Beeler-Reuter (MBR) parameters. Time increases from left to right and top to bottom and the frames are spaced every 25 ms. The tissue size is 6.2×6.2 cm and the contours are spaced every 20 mV. The wavelip calculated by Eq. (31) with $V_{iso} = -35$ mV is highlighted by a filled circle. The bottom right-hand frame shows a gray scale shading of V with repolarized tissue in black and the wavelip trajectory for the entire sequence from top to bottom.

membrane excitability and are not to be confused with the ellipses that are a simple contraction of circular cores.] In between these two extremes, a variety of flowerlike meander patterns with both inward and outward petals have been simulated. This evolution of meander patterns has been reported by Winfree in his survey of the FN model⁵⁸ by varying excitability [i.e., a parameter directly analogous to δ in Eqs. (21)–(22)]. It has also been demonstrated in BR kinetics by Krinsky, Efimov, and Jalife^{73–75} by changing the sodium conductance. The main difference is that subsequent arcs are more parallel to each other in BR than FN for high excitability (i.e., cores appear more linear in BR and more triangular in FN). This evolution is also reproduced by the three-current model as shown in Fig. 7. Krinsky *et al.* have argued that this linear structure should be present when the radius r of the pivot turn of the wavefront inbetween arcs, which

decreases with increasing excitability, is much smaller than the rotor wavelength λ , and circular cores when $r \sim \lambda$. They have also argued that the linear cores should rotate slowly at a rate $\sim r/\lambda$. Although heuristic, these arguments work reasonably well in practice and account qualitatively for the variation of core morphologies in Fig. 5. The cores of MLR-I and GP are more linear than the MBR core because of the larger sodium conductance in MLR-I than MBR, and hence smaller r . Furthermore, the line of block rotates faster in GP than MLR-I because of the smaller wavelength (i.e., smaller minimum APD of the APD restitution curve.)

A theory of linear cores still remains to be developed. At present, meander is only analytically understood in the opposite weakly excitable limit, either for large core radius where an equation of motion for the wavelip has recently been derived,⁷⁷ or near the codimension-2 point where the

onset of meander coincides with the transition line from inward to outward petals.^{78,79}

On the experimental side, current mapping methods do not allow characterization of the meander patterns with the same resolution as in numerical simulations or BZ experiments.^{80,81} Despite this limitation, progress has recently been made in identifying the transient meander patterns with both inward and outward petals of spiral waves that only last a few cycles.⁸² Also, reentry around lines of blocks that extend 1–2 cm seem commonly observed during reentry. They have been seen by Dillon *et al.*⁸³ and other groups since then (see for example Fig. 7 in Ref. 73 and Fig. 6 in Ref. 10). Davidenko *et al.* have also distinguished elliptical and linear cores in different sheep preparations (also Fig. 7 in Ref. 73). All of these observations seem to support, at least qualitatively, the existence of linear cores in normal myocardium. However, the transition from linear to circular core with varying excitability largely remains to be experimentally demonstrated.

The length of the linear core (~ 1 cm) and average period (~ 100 ms) come out in the right ball park for the model parameters fitted to the GP data, whereas for either MBR or MLR-I these two quantities are both larger (3–5 cm and 200 ms, respectively) than typically observed experimentally. This is due to the fact that the APD restitution curve terminates at a shorter APD in the GP data, and hence leads to a smaller wavelength, while still rising sufficiently gradually with increasing DI to forbid instabilities. It therefore seems reassuring that the model parameters that provide the best fit to measured curves *in vivo* produce about the right core length and period.

All the restitution curves fitted here, except the one for BR, do not produce spiral wave breakup in 2D. If we believe the GP data of Fig. 3 to be representative of normal myocardium (probably a better guess than what any of the current ionic models produce), then we may be tempted to speculate that the type of VF produced by 2D wave breakup mechanisms tied to restitution^{49,50,54} are only relevant for tissues with somewhat altered electrophysiology, perhaps as in in the experiment of Garfinkel *et al.*¹⁰ There is, however, insufficient restitution data at present to prove or disprove this speculation.

In summary, current ionic models and the limited amount of existing experimental data indicate, but do not prove, that reentry in *normal* myocardium is stable in 2D. The restitution curve of BR, which produces wavebreaks in 2D^{49,50} is anomalously steep because of its too slow Ca kinetics and low Na conductance. Speeding up this kinetics or increasing this conductance both tend to stabilize reentry in BR. Experimental curves also seem insufficiently steep to cause wavebreaks. Activation wavefronts in myocardium generally rotate along a line of block that is distinct from elliptical cores that describe tissue with a reduced excitability. This distinction, although clear in model simulation, remains to be better established experimentally since it is not always simple to distinguish highly contracted ellipses from the lines of block that would already be present in an isotropic medium.

VI. CHARACTERIZATION OF VORTEX LINES AND TWIST

One practical way to identify the spiral wave tip in 2D is to arbitrarily choose a single isopotential line of constant membrane potential, $V(\mathbf{r}, t) = V_{\text{iso}}$, where $\mathbf{r} = x\mathbf{x} + y\mathbf{y}$ is the position vector, to represent the boundary between depolarized and repolarized regions of the tissue, as when hand drawing a spiral wave. The wave tip can then be defined as the point where the excitation wavefront meets the repolarization waveback of the action potential, or equivalently as the point of zero normal velocity along this boundary. It is simple to show that this point is the intersection point of the lines $V = V_{\text{iso}}$ and $\partial_t V = 0$, defined by the coordinates $(x_{\text{tip}}, y_{\text{tip}})$ of the vector $\mathbf{R} = x_{\text{tip}}\mathbf{x} + y_{\text{tip}}\mathbf{y}$ that satisfy:

$$V(\mathbf{R}, t) - V_{\text{iso}} = \partial_t V(\mathbf{R}, t) = 0. \quad (31)$$

In FN-type models, both the wavefront and the waveback are thin boundary layers of width ϵ such that different values of V_{iso} (chosen between the resting and peak membrane potentials) lead to meander trajectories that are all within a distance ϵ of each other, and therefore practically indistinguishable on the scale of the core. Meander patterns depend more markedly on the choice of V_{iso} for ionic models (BR and others) with a spatially more diffuse waveback. The basic morphology of a meander pattern (e.g., linear versus circular and the angle between petals) remains independent of the choice of V_{iso} .

Equation (31), which defines the wavetip as a point in 2D, defines the *instantaneous* vortex line in 3D as the intersection of two surfaces. This line is denoted here by $\mathbf{R}(s, t) = x(s, t)\mathbf{x} + y(s, t)\mathbf{y} + z(s, t)\mathbf{z}$, where s is the arclength along the line and $\mathbf{t}(s, t) \equiv \partial_s \mathbf{R}(s, t) / |\partial_s \mathbf{R}(s, t)|$ is the unit vector locally tangent to the filament. The filament curvature κ and the torsion ν are defined by the Frenet–Serret equations $\partial_s \mathbf{t} = \kappa \mathbf{n}$ and $\partial_s \mathbf{n} = -\kappa \mathbf{t} + \nu \mathbf{b}$, where \mathbf{n} and \mathbf{b} are the normal and binormal directions to the filament in the local Frenet–Serret frame.

In order to calculate twist, it is useful to define the vector field

$$\mathbf{N} = \frac{\nabla V}{|\nabla V|} \Big|_{\mathbf{r}=\mathbf{R}}, \quad (32)$$

which points parallel to the gradient of membrane potential at the point or line of phase singularity. In 2D, \mathbf{N} is simply the unit vector perpendicular to the the wavetip trajectory. The angular frequency of rotors is just $\omega = |d\mathbf{N}/dt|$ for non-meandering spiral waves. In contrast, for meandering spirals with elongated cores, $|d\mathbf{N}/dt|$ is large when the excitation wavefront rotates rapidly $\sim 180^\circ$ twice per period, and small when it travels along an arc of conduction block in between rotations.

In 3D, $\mathbf{N}(s, t)$ becomes a vector field along the vortex line that is locally perpendicular to the tangent $\mathbf{t}(s, t)$ and hence lies in the plane spanned by \mathbf{n} and \mathbf{b} . The twist $W(s, t)$, which is distinct from the torsion, is then the scalar field

$$W(s, t) = [\partial_s \mathbf{N}(s, t) \times \mathbf{N}(s, t)] \cdot \mathbf{t}(s, t), \quad (33)$$

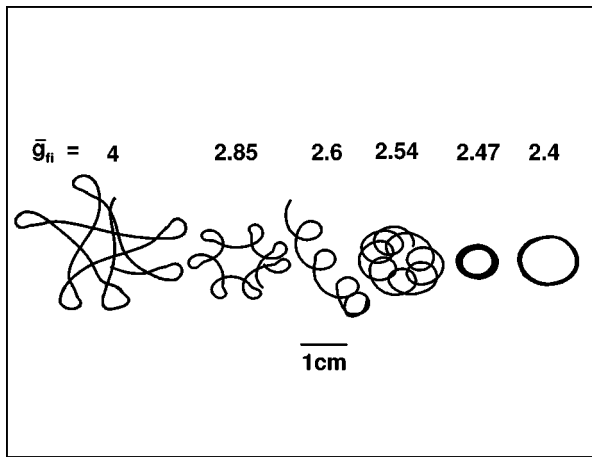


FIG. 7. Wavetip trajectories for the MBR parameter set in a 2D isotropic tissue obtained by varying the conductance parameter \bar{g}_{fi} of the fast inward (sodium) current.

which measures the rate at which \mathbf{N} rotates in the plane perpendicular to $\mathbf{t}(s, t)$ as one moves along the filament.³⁴ A numerical algorithm to calculate the filament position and twist according to Eqs. (31), (32), and (33) is described in Appendix B.

We have also found useful to define the transmural twist amplitude $W_t = \Delta\phi/S$ where

$$\Delta\phi = \sin^{-1} |\mathbf{N}^{\text{endo}}(t) \times \mathbf{N}^{\text{epi}}(t)| \quad (34)$$

is the angle between the normal directions on the epicardium and the endocardium, as well as to define the Euclidean distance

$$L_E(t) = [(x_1(t) - x_2(t))^2 + (y_1(t) - y_2(t))^2 + S^2]^{1/2} \quad (35)$$

between the breakthrough points of the same vortex line (wavetips) on the epicardium (x_1, y_1) and endocardium (x_2, y_2) . These quantities have the advantage that they are measurable experimentally by simultaneously mapping both surfaces. $L_E(t)$ is by definition always smaller or equal to the total filament arclength defined by $L(t)$ and the difference between these two lengths is a measure of the curving of the vortex line intramurally.

Laws of filament motion have been analytically derived for reaction-diffusion models.^{36,38,39} These laws have been derived under the assumptions that: (i) the medium is isotropic; (ii) spiral waves do not meander; and (iii) the filament moves on space and time scales that are much larger than the core size and rotor period, respectively. However none of these assumptions generally apply to the heart. Scroll waves typically meander in a rotationally anisotropic medium on a core size at least comparable to the wall thickness. In this case, it becomes crucial to understand the motion of the instantaneous line of phase singularity on the *inner scale* of the core and on a time scale much shorter than the period. Weak excitability may be one exception where assumptions (ii) and (iii) may be satisfied because spiral waves tend to rotate rigidly around a small core, but even in this case assumption (i) is violated. Therefore, there is presently no proper analytical theory to reliably describe vortex line motion in ventricular muscle.

VII. COMPUTATIONS

We present in this section selected simulation results that best serve to illustrate the answers to the questions raised at the end of the review section. We restrict our attention to parameters of the three-current model that reproduce the restitution properties of the Beeler-Reuter model with speed-up calcium (i.e., MBR column in Table I). The other models with stable reentry patterns in 2D (MLR-I and GP) yield similar results that will be presented elsewhere. In order to also explore the role of the excitability of the tissue we report results for $\bar{g}_{fi}=4$, corresponding to normal sodium conductance of Beeler-Reuter, and the reduced value $\bar{g}_{fi}=2.47$. Recall that, in an isotropic medium, the higher value yields the complex meander trajectory of the wave tip along successive arcs of conduction blocks, and rapid pivot turns around small outward petals in between, and the lower value yields steady-state rotation around a circular core of unexcited tissue (Fig. 7). This allows us to contrast the role of rotational anisotropy in these two opposite regimes of re-entry.

A. Choice of parameters

The ratio of conduction velocities c_{\parallel}/c_{\perp} varies typically between 2 and 3, which corresponds to a ratio of D_{\parallel}/D_{\perp} between 4 and 9. We used here a ratio of 5 with $D_{\parallel}=1 \text{ cm}^2/\text{s}$ and $D_{\perp}=D_{\perp 1}=D_{\perp 2}=1/5 \text{ cm}^2/\text{s}$. For $\bar{g}_{fi}=4$, the maximum conduction velocity is 42 cm/s parallel to the fiber axis [Fig. 3(b)] and 19 cm/s in the two perpendicular directions. The range of wall thickness (S) and fiber rotation rate (θ_z) was chosen on the basis that for, $\Delta\theta=120^\circ$, a 1 cm LV wall thickness yields $\theta_z=12^\circ/\text{mm}$, and a 4 mm RV wall thickness yields $\theta_z=30^\circ/\text{mm}$. We therefore chose to vary S between 1 mm and 1 cm for four different fiber rotation rates $\theta_z=6^\circ/\text{mm}$, $9^\circ/\text{mm}$, $12^\circ/\text{mm}$, and $30^\circ/\text{mm}$. This choice covers approximately the region of the $S-\theta_z$ plane that could be accessed experimentally by rendering electrically inactive a fractional depth of tissue. We varied S at constant θ_z by removing epicardial layers. So all results are always shown as viewed from the top of the exposed transmural layer. This is purely a matter of choice and removing endocardial layers would have been equivalent since we do not take into account the Purkinje network.

The simulations were carried out using the algorithm described in Sec. III and Appendix A on cubic lattices with $200 \times 200 \times N_z$ and $300 \times 300 \times N_z$ grid points. The grid spacings along x and y were chosen as $\Delta x = \Delta y = \Delta = 0.031 \text{ cm}$ (so these lattices correspond to slabs of width \times length \times height equal to $6.2 \times 6.2 \times N_z \Delta z \text{ cm}$ and $9.3 \times 9.3 \times N_z \Delta z \text{ cm}$, respectively.) The time step was chosen equal to $\Delta t = 0.25 \text{ ms}$. These values of Δ and Δt give a maximum propagation speed parallel to the fiber axis that is a few percent smaller than it would be in the fully resolved continuum limit. The spacing Δz between layers was decreased for larger θ_z to keep the jump in angle between layers in the range of 1° – 3° . We chose $\Delta z = \Delta$ for $\theta_z=6^\circ/\text{mm}$ and $\theta_z=12^\circ/\text{mm}$, and $\Delta z = \Delta/3$ for $\theta_z=30^\circ/\text{mm}$. S was varied between 1 mm and 10 mm by varying N_z between about 4 and 40 for $\Delta z = \Delta$ and 12 and 120 for $\Delta z = \Delta/3$. The convergence of the results was tested by repeating some simulations for various S and θ_z with

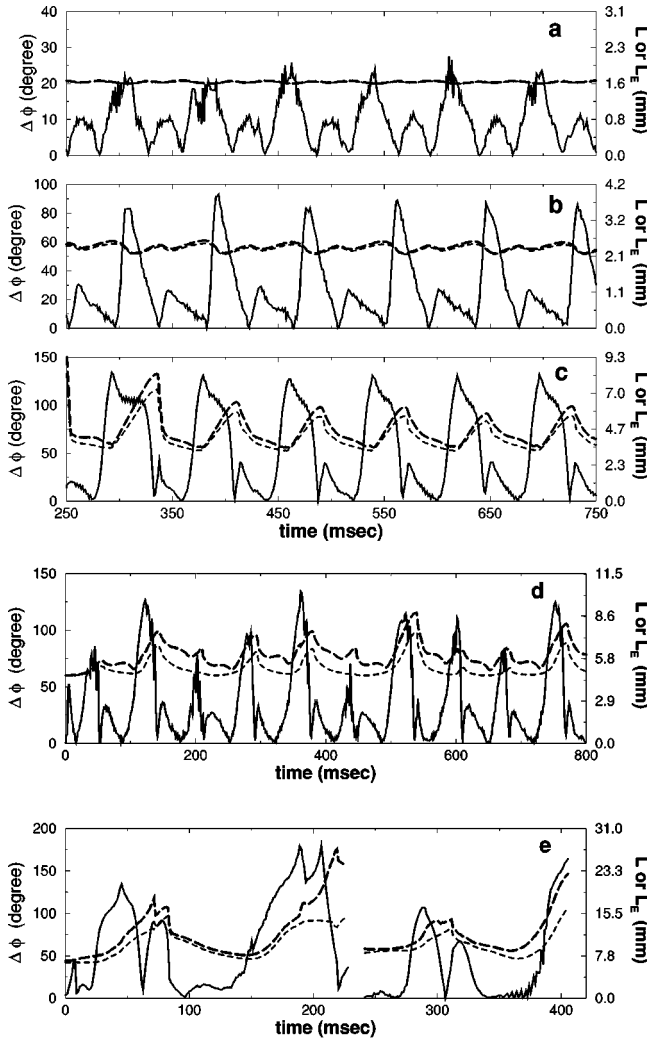


FIG. 8. Plots illustrating the relaxation oscillations of the transmurals twist angle $\Delta\phi$ (solid line), the total filament length L (thick dashed line), and the Euclidean distance L_E (dashed line) between wave tips on the epicardium and endocardium. All plots are for a fiber rotation rate $\theta_z = 12^\circ/\text{mm}$. Plots (a)–(d) are for $\bar{g}_{ri} = 2.47$ and $S = 1.6$ mm (a), 2.2 mm (b), 3.1 mm (c), and 4.65 mm (d). Plot (e) is for $\bar{g}_{ri} = 4$ and $S = 6.2$ mm. The plot in (e) is interrupted when the vortex line collides with the surface, as shown in the corresponding Fig. 12, and is continued after the half-ring created by this collision has vanished.

smaller Δ , Δz , and Δt . These test yielded quantitative differences of a few percent but no qualitative change in wave behavior. So we do not believe that any aspects of our results are produced by lattice artifacts.

We used as initial condition in all the simulations an untwisted scroll wave with a straight filament obtained by stacking along the z -axis identical two-dimensional spiral waves, or identical two-dimensional broken plane waves. A typical simulation of 1 s of real time for a lattice size of $300 \times 300 \times 100$ took on average 20 h of CPU time on a ≈ 100 MFLOPS workstation. The interesting instabilities occurred during the first second but longer runs of up to 3 s were occasionally carried out for isolated parameter values.

B. Results and main features

We show in Fig. 8 plots of the transmurals twist angle

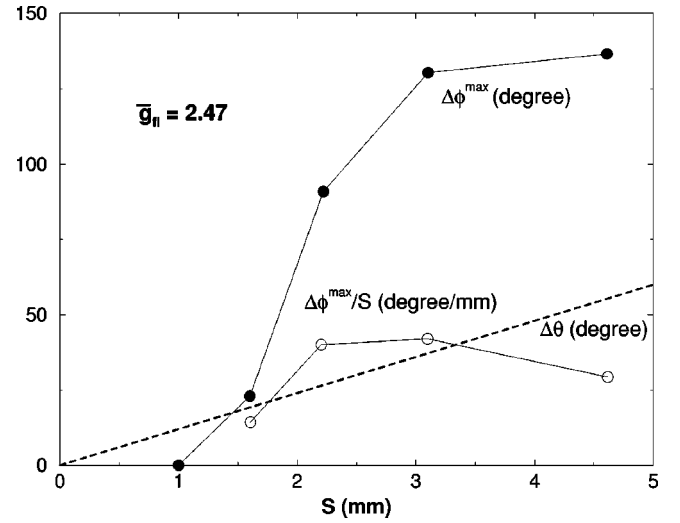


FIG. 9. Plot of the peak oscillation amplitude of the transmurals twist angle $\Delta\phi^{\max}$ (filled circle) and twist $\Delta\phi^{\max}/S$ (open circles) as a function of wall thickness S for $\bar{g}_{ri} = 2.47$. The total angle $\Delta\theta$ of fiber rotation is plotted as a dashed line for comparison.

$\Delta\phi(t)$ versus time, which recall is the angle between the normals (wavefront directions) on the epicardium and endocardium and differs from the fixed total angle of fiber rotation $\Delta\theta = \theta_z S$. The transmurals twist amplitude W_t can then be simply read from these plots by dividing $\Delta\phi(t)$ by the corresponding S . We also plot versus time on the same graphs the Euclidean distance $L_E(t)$ between the wavetips on the epicardium and endocardium and the total filament length $L(t)$. Several plots are shown for various wall thicknesses (see caption) and the two different excitabilities. In Fig. 9 we plot versus S the peak oscillation amplitude of twist angle ($\Delta\phi^{\max}$) and twist ($W_t^{\max} = \Delta\phi^{\max}/S$), as well as the total angle of fiber rotation $\Delta\theta = \theta_z S$.

The main features to be noted in these two plots are:

- (1) $\Delta\phi(t)$ undergoes nonlinear oscillations with a relaxational character between zero and some peak value $\Delta\phi^{\max}$, rather than smooth oscillations around some mean value.
- (2) The filament length also undergoes relaxation oscillations with a peak amplitude shifted in time with respect to the one of twist, i.e., the length is about maximum when the twist reaches zero after a large amplitude oscillation.
- (3) The basic period of oscillation is half of the rotor period, i.e., there are two main peaks of per rotor period for $\bar{g}_{ri} = 2.47$ in the range of S where oscillations are periodic. For the meandering case there is one main peak per outward petal of the meander path.
- (4) $\Delta\phi^{\max}$ increases rapidly with S , above about 1 mm here, and saturates in the range $\approx 100^\circ - 120^\circ$ for $\bar{g}_{ri} = 2.47$, and $\approx 150^\circ - 200^\circ$ for $\bar{g}_{ri} = 4$. Consequently, $\Delta\phi^{\max}$ can become much larger than $\Delta\theta$ with increasing S . Moreover, the average twist $\Delta\phi^{\max}/S$ first rises rapidly with S up to some maximum value and then decreases for larger S .
- (5) For the reduced excitability $\bar{g}_{ri} = 2.47$ where there is no

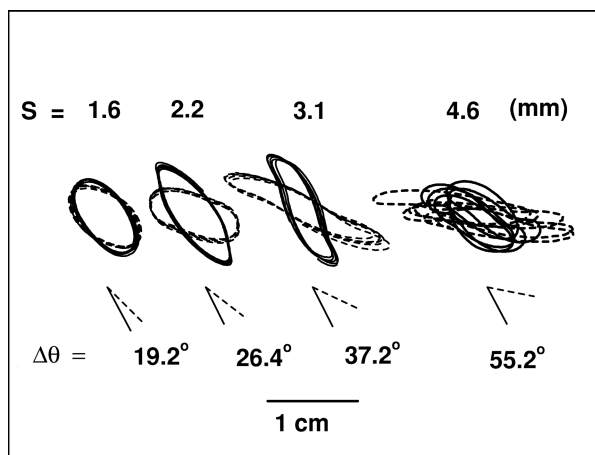


FIG. 10. Plot of the wavetip trajectories on the endocardium (solid line) and epicardium (dashed line) for different wall thicknesses, $\bar{g}_H = 2.47$, $\theta_z = 12^\circ/\text{mm}$. The fiber direction on each surface is indicated as in Fig. 2. For the same excitability, the wavetip trajectory is a simple ellipse in 2D. Note that the trajectories on the epicardium and endocardium depart progressively from ellipses with increasing S and their major axes become rotated from each other by an angle that is comparable to the transmural angle $\Delta\theta = \theta_z S$ of fiber rotation. For the larger thickness the wavetips meander on each surface.

meander in 2D, the character of the oscillation changes from periodic to aperiodic with increasing S (i.e., they become aperiodic for S larger than about 4 mm here). [We have not attempted here to determine how the transition from periodic to aperiodic behavior takes place or to measure a Lyapounov exponent to determine if the aperiodic regime is truly chaotic. This would require longer simulation runs.] For the parameter $\bar{g}_H = 4$ where complex meander is already present in 2D, the twist oscillations are aperiodic for all S where they are visible, as one would naively expect since the 2D meandering motion is already somewhat aperiodic. Moreover the oscillations are narrower (i.e., more sharply peaked in time) for the meandering than for the nonmeandering case.

For the lower excitability, we plot in Fig. 10 the trajectories of the wavetip on the endocardium and epicardium for various S . The main features to be noticed here are how the epi- and endo-trajectories of the wavetip become rotated with respect to each other with increasing S and $\Delta\theta$, and how they differ from the purely 2D anisotropic trajectory for the same parameters [i.e., the isotropic trajectories of Fig. 7 contracted along the axis perpendicular to the fiber axis by $(D_{\perp 1}/D_{\parallel})^{1/2}$]. This difference is particularly evident for the reduced excitability ($\bar{g}_H = 2.47$) where the epi- and endo-trajectories can be seen to depart progressively from ellipses with increasing S . Furthermore, the onset of aperiodic oscillations at larger S for $\bar{g}_H = 2.47$ is associated with the onset of a more complicated motion of the wave tip on the epicardium and the endocardium. So it is interesting to note that, within some broad definition where meander depicts generally unclosed quasiperiodic or chaotic trajectories, one can have rotational-anisotropy-induced meander in a parameter range where motion is simply periodic in 2D.

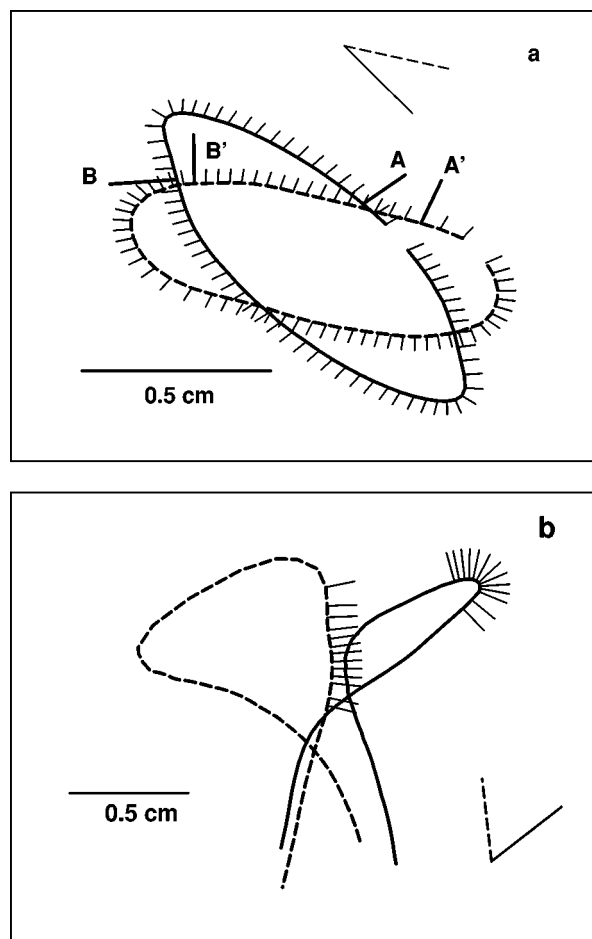


FIG. 11. Plot of the trajectories of the wave tip on the endocardium (solid line) and epicardium (dashed line) for $\theta_z = 12^\circ/\text{mm}$ and (a) $\bar{g}_H = 2.47$ and $S = 2.2$ mm, (b) $\bar{g}_H = 4$ and $S = 3.1$ mm. The trajectories correspond to the time intervals $340 \leq t \leq 510$ ms in (a) and $50 \leq t \leq 80$ ms in (b), which can be correlated with the oscillations in Fig. 8(b) and (e), respectively. The normal directions N are represented by tick marks spaced every 2.5 ms. In (a) $A(A')$ and $B(B')$ indicate the wavefront positions on the epicardium (endocardium) when $\Delta\phi$ is at its two maxima with the highest one at $B(B')$. Note that in (b) the wavefront on the epicardium has made a leading pivot turn by 152° while the lagging wavefront on the endocardium has only rotated by 24° during the same interval of time.

Next, Fig. 11 provides the essential bridge between Figs. 8 and 10. It is intended to show how the motions of the wavetips on the epicardium and endocardium gives rise to the oscillations of twist amplitude and filament length in Fig. 8. For this purpose we choose a certain time interval $t_1 \leq t \leq t_2$ (see caption) that corresponds to one oscillation of twist in Fig. 8. We then plot the wavetip trajectories on the epicardium and endocardium that correspond to this time interval. Finally, we indicate the successive positions of the wavetips along the trajectories by the normal directions N (tick marks) at equal intervals of time. By counting the number ticks along each trajectory (top and bottom) one can pinpoint the relative positions and orientations of the activation wavefronts on the epicardium and endocardium at different times and correlate their motions with the oscillation of Fig. 8. The main feature to be noticed in these plots is that the rapid pivot turn of the wavefront on one of the two bounding surfaces (endocardium here) *leads in time* the pivot turn of

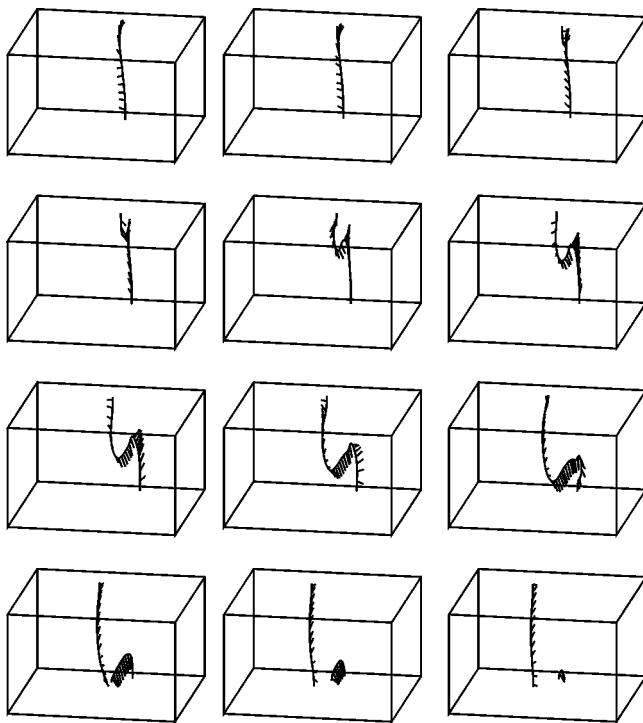


FIG. 12. Three-dimensional snapshots of the vortex line and the normals \mathbf{N} for $\bar{g}_{\text{fi}}=4$, $\theta_z=12^\circ/\text{mm}$, and $S=6.2\text{ mm}$. The sequence starts at $t=170\text{ ms}$ and can be correlated with the oscillation of the transmural twist angle in Fig. 8(e). Frames are spaced every 6.25 ms. Time increases from left to right and top to bottom. The scale of the z -axis is greatly magnified in comparison to the other axes to visualize the filament. In the right-hand-most frame of the third row just before collision (ninth frame) the filament length is $\approx 18\text{ mm}$ or about three times S . Note that regions of large twist along the vortex line coincide with regions of large curvature.

the wavefront on the other surface (epicardium here). For $\bar{g}_{\text{fi}}=2.47$, the rapid pivot turns occur when the wavefront travels along the highly curved part of the distorted elliptical trajectories that are at opposite ends of their major axes, whereas for $\bar{g}_{\text{fi}}=4$, they occur when the wavefront travels along the small outward petals.

Next, Figs. 12–15, illustrate the intramural dynamics of the vortex line and its twist for the range of S where the oscillations become large. The vortex line and the normals \mathbf{N} are shown at equal intervals of time during one of the oscillation of Fig. 8(e). The voltage activity on the epicardium and the endocardium corresponding to frames 4 to 11 is shown in Fig. 13. The local twist angle, $\phi(s, t) \equiv \int_0^s ds' W(s', t)$, is plotted as a function of the arclength position s along the filament in Fig. 14 for the times that correspond to frames 4 to 9 in Fig. 12 (reading from left to right and top to bottom). The important features to notice in these figures are that:

- (i) The filament winds itself just below the surface of the leading pivot turn of the wavefront and then unwinds at the opposite surface by the transmural propagation along the filament of a localized region of large twist referred hereafter as a twiston.⁸⁴
- (ii) One can estimate from Fig. 14 that the maximum local twist is $\approx 50^\circ/\text{mm}$ (i.e., 100° jump in angle divided by a 2 mm gap between flat regions of small

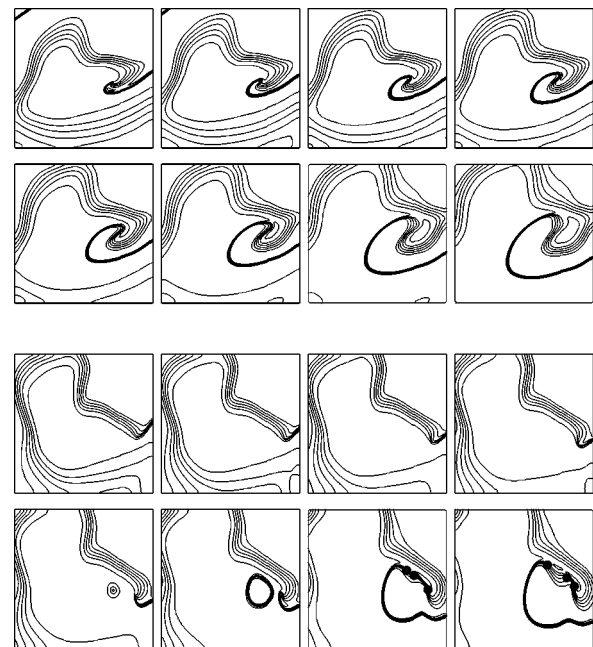


FIG. 13. Contour plots of V at intervals of 20 mV on the epicardium (a) and endocardium (b) corresponding to frames 4 to 11 in Fig. 12. The end points of vortex lines (wave tips) are shown by filled circles in the frames that follow the creation of a half-ring.

- angle change) and that twistons move at a speed that is roughly Mach 1 compared to $c_{\perp 2} \approx 20\text{ cm/s}$ here.
- (iii) The filament is morphologically unstable. This instability is tied to the fact that localized regions of twist coincide with regions of large filament curvature and the filament can lengthen to several times the wall thickness as a result.
- (iv) The collision with the surface of such a region of high curvature leads to the creation of a half-ring (full ring with the mirror image through the boundary). It is important to emphasize that no new length of filament is actually created at the instant of collision. The newly formed half-ring is just a cut out segment of the original filament.

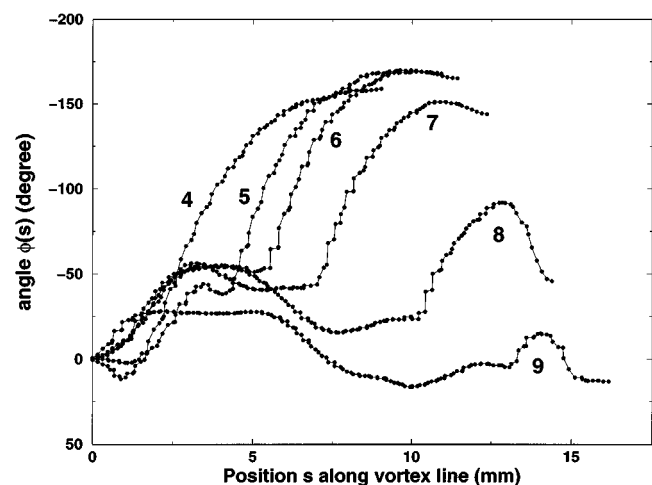


FIG. 14. Plots of the twist angle ϕ vs the arclength position s along the filament corresponding to the two middle rows (frames 4–9) in Fig. 12.

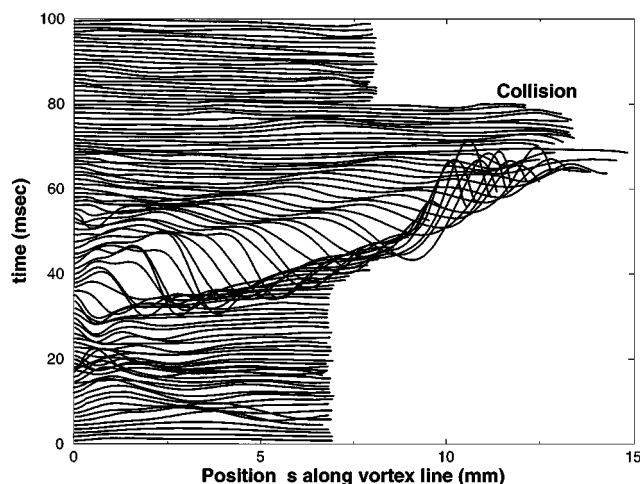


FIG. 15. Spatiotemporal plots of the vortex twist $W(s)$ stacked in time from bottom to top every 1.25 ms for $\bar{g}_H=4$, $S=7.5$ mm, and $\theta_z=12^\circ/\text{mm}$. This plot shows the transmural propagation of a twiston created about 1 mm below the epicardium. The speed of propagation can be extracted directly from the slope of the line of crest in this plot and is about 20 cm/s. Note that the vortex line elongates as the twiston propagates. The instant of collision with the endocardium is marked.

The propagation of a twiston is further illustrated in Fig. 15 where we show a spatiotemporal plot of the local twist $W(s,t)$ as a function of the arclength position s along the filament for $S=7.5$ mm and $\bar{g}_H=4$, i.e., different snapshots of $W(s,t)$ vs s are shown at various times shifted along the ordinate. The twiston appears as a localized excitation that propagates from left to right (epicardium to endocardium). An interesting feature, already present in Fig. 14, is that the propagation of this pulse is accompanied by a lengthening of the filament. Consequently the filament length is maximum about when unwinding is completed. Examination of other plots similar to Fig. 15 reveal that the spatiotemporal dynamics along the filament can become more complex. Twistons are not always created and annihilate at boundaries. Two twistons sometimes combine to form one or a single twiston can suddenly split into two twistons propagating in opposite directions.

The next series of plots focuses on the transition from VT to VF as a function of S and θ_z for the normal excitability parameter $\bar{g}_H=4$. We have found useful to distinguish three dynamical states, which we observe with increasing S at fixed θ_z : (i) a globally stable VT-like state with a single chaotically meandering filament but no creation of new filaments, (Note that, contrary to here, dynamical states with a single rotor have been categorized as VF by other authors^{45,46} based on the fact that they can produce a complex ECG. Purely as a matter of definition, we use the term VF throughout this paper to refer to a spatiotemporally chaotic wave state with multiple rotors, independently of the complexity of the ECG.) (ii) a state intermediate between VT and VF where the wave dynamics remains dominated on average by a single transmural filament, but with occasional collisions leading to the *transient* formation of a half-ring filament that vanishes at the boundary where it is created (Fig. 12); (iii) a fully developed VF state with an average number of filaments substantially larger than one. In this

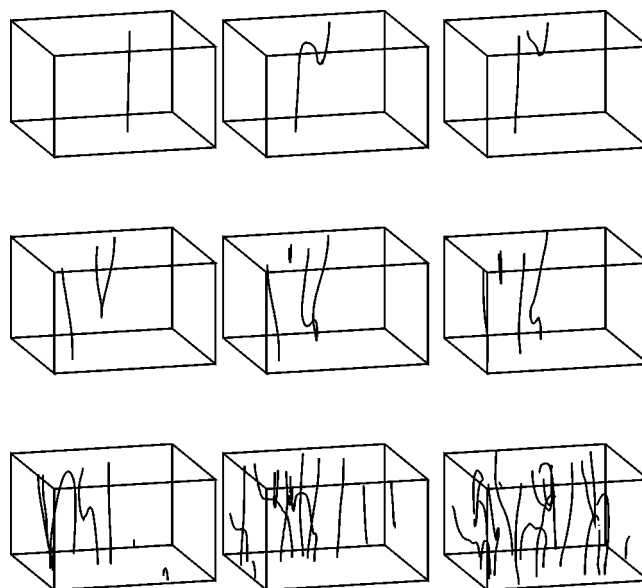


FIG. 16. Three-dimensional snapshots showing the main creation events of vortex lines that lead to the decay of VT into VF for $\bar{g}_H=4$, $\theta_z=12^\circ/\text{mm}$, and $S=6.2$ mm. The snapshots are shown at $t=0, 405, 409.5, 459, 472, 497, 654, 785$, and 950 ms with time increasing from left to right and top to bottom. The scale of the z -axis is greatly magnified as in Fig. 12.

state filaments are continuously being created by sectioning of pre-existing filaments in two parts due to collision with the surface, the pinching off of a long filament in the interior of the muscle, or the spontaneous creation of a vortex ring. They are continuously being destroyed by vanishing at boundaries or merging with other filaments (e.g., the merging of a half-ring and transmural filament). Figure 16 illustrates how the transition from VT to VF occurs for $\theta_z=12^\circ/\text{mm}$ and $S=6.2$ mm. Three-dimensional snapshots of the filaments are shown at nine different instant of times chosen to illustrate the complex sequence of events that leads to a fully turbulent wave behavior. In the first three frames filament creation occurs as described above by the collision of a twiston with one surface (endocardium here). However, the newly created half-ring does not vanish but grows instead to hit the endocardium and create two more filaments. The following sequence of frames would require many more frames in between to render all the details of each filament creation and annihilation events (which are not essential to show here). The net product is the complex filamentary state (with about 16 filaments) in the bottom right frame.

Figure 17 shows the electrical activity on the epicardium and the endocardium for the same instants of time corresponding to the frames in Fig. 16. This activity is imaged by showing contour plots of the transmembrane voltage and the places where filaments breakthrough on these surfaces are indicated by solid circles. The last three frames are repeated at the bottom of each panel using a gray scale shading showing depolarized (repolarized) regions of the tissue in white (black).

We compare in Fig. 18 recordings of V at one point on the epicardium ($x=3.1$ mm and $y=1.5$ mm) for 3.5 s of VT ($S=3.1$ mm) and VF ($S=6.2$ mm). Then, in Fig. 19 we show the histograms of APD distribution obtained from a

total of 4800 simultaneous recording points uniformly distributed on the epicardium, midwall, and endocardium. The main feature to notice here is that, for the VT, the distribution of APD is centered around the mean value of APD for the hyper-meandering 2D rotor. In contrast, for VF, the distribution is centered around a smaller APD and is comparatively much broader. Random bursts of shortened APD can be clearly seen in Fig. 18. We infer that this difference of histograms is a direct consequence of the large number of vortex lines present in VF. This is because excitations associated with the passage of a vortex line near a recording point reexcite the membrane at a much smaller peak value of V . This reduced peak value then yields a short APD since: (i) the slow inward current is not activated to prolong the APD; and (ii) it takes a shorter time to repolarize from a reduced peak value. So there is a direct correlation between the vortex line density and the shape of the APD distribution.

Finally, all our simulation results for the normal excitability are plotted in Fig. 20 that is similar to Fig. 1 of Winfree in Ref. 33. It is one of the key figure to be discussed in the next section in relation to experiment.

VIII. DISCUSSION

A. Interpretation of the results

1. Winding, unwinding, and twistons

Figure 9 shows that the transmural twist angle $\Delta\phi$ has a peak amplitude that exceeds the angle of fiber rotation $\Delta\theta$ already for small wall thickness. For the maximum twist amplitude of about $50^\circ/\text{mm}$, and the layer spacing of 0.031 cm used in our simulations, the maximum jump in phase angle of the rotor between layers is about $15^\circ/\text{mm}$. However, we repeated the simulations with a layer spacing twice smaller and found nearly identical results within a few percent, demonstrating that these results are not artifacts of the discretization, but dynamical features of the continuum limit.

One immediate conclusion is that the naive estimate of Sec. II, which equates $\Delta\phi$ and $\Delta\theta$, turns out to be grossly incorrect. Also, the twist amplitude is found to be only negligible below about 1 mm here, which is much smaller than the 5 mm or so estimate of S_{\min} obtained by equating the diffusive decay time t_d with the rotor period. Moreover, twist decays propagatively rather than diffusively.

To understand why these estimates fail, and what the more correct ones are, we need to examine the origin of these oscillations. While one would expect oscillations to be present because the fiber rotation breaks the underlying rotational symmetry, one would not necessarily expect large amplitude relaxation oscillations. To see why those occur, let us discuss first the nonmeandering case of reduced excitability ($\bar{g}_{\text{fi}} = 2.47$) for $S = 2.2\text{ mm}$, which is simpler to interpret and already contains the basic mechanism of oscillation. In this case, the trajectories of the wavetips on the endocardium and epicardium are only slightly distorted ellipses whose major axes are rotated from each other by an angle, defined here as α , which is roughly equal to $\Delta\theta$ as can be seen in Fig. 10. So, estimating that $\alpha \approx \Delta\theta$ is about right, but the key point is that α is not the transmural twist angle. This is because the rapid pivot turn of the wavefront on the epicardium *leads* in time

the pivot turn on the endocardium for counterclockwise rotation and vice versa for clockwise rotation. This can be clearly seen in Fig. 11(a) where the wavetips and normals \mathbf{N} on the epicardium (B) and endocardium (B') are shown at the instant of time where $\Delta\phi$ is maximum during one oscillation in Fig. 11(b). At this instant the wavefront on the epicardium has completed its pivot turn on the curved section of the distorted elliptical trajectory, whereas the wavefront on the endocardium is only initiating its turn. Consequently, $\Delta\phi$ is much larger than α at this instant. With no time delay between pivot turns on both surfaces, $\Delta\phi$ would be about constant in time and equal to α . The same mechanism holds true for the higher excitability as shown in Fig. 11(b). The main difference is that now the leading pivot turns occur on the small outward petals of the contracted meander trajectories in between arcs of blocks.

This winding mechanism makes it possible to understand semi-quantitatively a number of the features of the oscillations mentioned in the last section. We only mention here the main ones and others are straightforward to deduce by examining the results. In a regime where the oscillations become strongly nonlinear, the twist angle rises from zero to its maximum value in the range of $\approx 10\text{--}20\text{ ms}$. This corresponds approximately to the time t_{piv} to make a pivot turn. The main peaks of the oscillations occur twice per period because, for reduced excitability, there are two highly curved sections of the trajectories at opposite ends of the major axes of the distorted ellipses, and hence two fast pivot turns per period. It is also simple to deduce that the alternate smaller peaks must exist as a consequence of the fixed angle (α) between trajectories and the epi-to-endo time delay of wavefront rotation. For normal excitability, there is one pivot turn at the end of each journey of the wavetips along an arc of block, and therefore also two main peaks per period for linear cores. A simulation of MLR-I (or MBR with higher \bar{g}_{fi}) shows regular oscillations with two peaks per period. Those of MBR with $\bar{g}_{\text{fi}} = 4$ shown here are more irregular because the meandering behavior is itself already aperiodic. This is however a secondary aspect here.

For intermediate S , the peak of oscillation of the filament length, or the Euclidean distance L_E between wavetips, coincides with the minimum of twist angle after a large oscillation. Examination of the results shows that this is because the leading wavefront rushes ahead along its trajectory, either along an arc of block or a gently curved part of the distorted ellipse, after executing its turn, while the lagging wavefront pivots more slowly. Hence once the lagging wavefront has completed its turn, and $\Delta\phi$ is minimum, the filament has stretched to make L and L_E maxima. Note that L and L_E only remain close to each other for small S . For larger S , L and L_E start to depart from each other due to the twist-induced intramural curving of the filament.

Let us now turn to the issue of why the filament unwinds propagatively, rather than simply diffusively as observed for example in the BZ reaction,⁴² and assumed to be the case in the estimations of Sec. II. Two factors contribute to this difference. First, for S larger than about 2 mm , the pivot time t_{piv} becomes much shorter than the transmural diffusion time t_d . Thus twist is built-up far too quickly to allow smooth

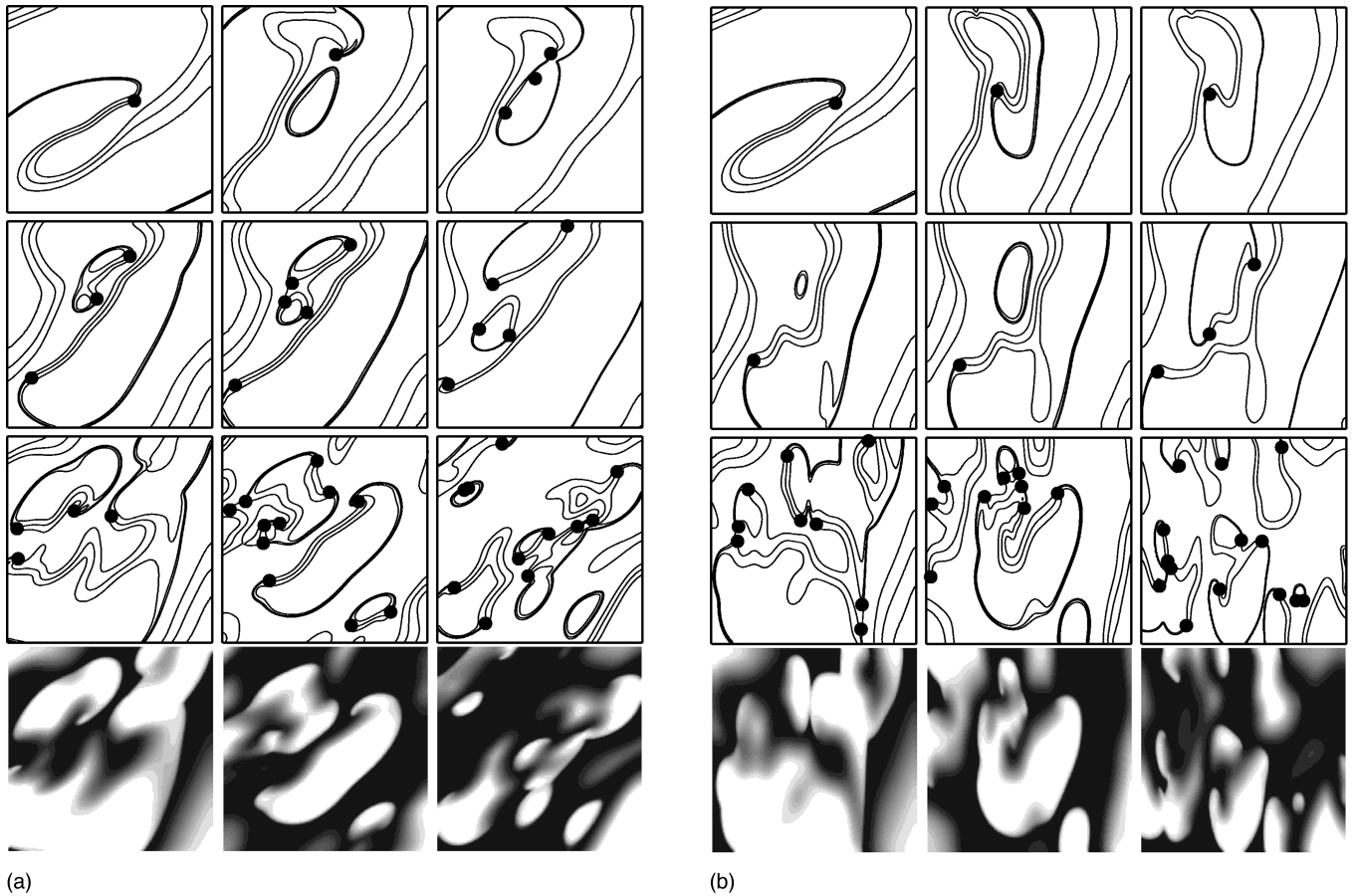


FIG. 17. Contour plots of V spaced every 30 mV on: (a) the epicardium, and (b) the endocardium corresponding to the sequence of frames in Fig. 16. End points of vortex lines on either surfaces are shown as filled circles. The bottom row is repeated with a gray shading showing polarized (black) and depolarized (white) regions of tissue.

diffusive unwinding. This is different in BZ because twist is built-up by a gradient of parameter over several rotation periods. Second, the twist amplitude is large enough for non-linear effects to become important and cause localized propagating excitations to develop.

We have used rather loosely the term twiston to describe such excitations because they are highly localized spatially along the filament and propagate transmurally at a speed comparable to the underlying wave speed. However, it is not entirely clear if twistons behave more like solitons or shock waves. The existing analyses of twist dynamics along straight vortex lines,^{38,39} although not strictly applicable here for the reasons discussed at the end of Sec. VI predict that twist is governed by Burger's equation, which supports shock wave solutions. Yet, our simulation results plotted in the plane of twist and position along the filament (Fig. 15) show a more soliton-like behavior that is reminiscent of solitary waves of helicoidal disturbance propagating along vorticity filaments in fluid turbulence.^{85,86} However, twistons here may not be pure solitons since they appear in some cases (other than Fig. 15) to spread spatially as they propagate. Analytical theories of twist dynamics in a rotationally anisotropic medium and more detailed simulations seem needed to describe these excitations and shine light on this issue.

2. New estimates

With the above mechanism in mind, we can return to crudely estimate the peak twist amplitude $\Delta\phi^{\max}$ and the thickness S_{\min} below which this amplitude should be negligible. Now using the fact that the time for twist build-up is of the order t_{piv} , and not the rotor period, we can modify our previous diffusive estimate by equating t_d and t_{piv} . This yields $S_{\min}^{\text{diff}} \approx \pi(D_{\perp} 2t_{\text{piv}})^{1/2}$ which is about 1.5 mm for $t_{\text{piv}} = 10$ ms and the present parameters. If we assume instead that twist decays propagatively, as our results demonstrate for larger S , we estimate that $S_{\min}^{\text{prop}} \approx c_{\perp} 2t_{\text{piv}}$ which is about 1 mm with $c_{\perp} \approx 10$ cm/s. A more detailed numerical study at small S would be necessary to determine which estimate is more appropriate but the important point here is that both are between 1 and 2 mm in good accord with our results. Thus twist is already relevant at a small thickness.

Next, we can crudely estimate that $\Delta\phi^{\max}$ should saturate at large S (Fig. 9) at a value approximately equal to the total angle of rotation of the wavefront during its pivot turn, ϕ_{piv} . In general, ϕ_{piv} will depend on the nature of the wavetip trajectories and the time delay between the pivot turns on the epicardium and endocardium. However, ϕ_{piv} is relatively simple to estimate in two limits. First, for normal excitability, the wavefront rotates by $\approx \pi$ in between jour-

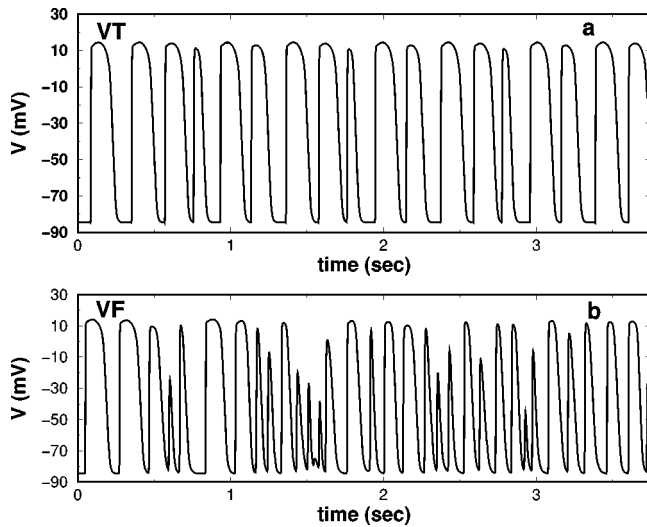


FIG. 18. Transmembrane voltage recordings of V from a point on the epicardium for: (a) VT with a single transmural vortex filament and $S = 3.1$ mm; and (b) VF with a large average number of filaments (10–20) and $S = 6.2$ mm. Other parameters are $\theta_z = 12^\circ/\text{mm}$ and $\bar{g}_{fi} = 4$.

neys along arcs of blocks. Second, for reduced excitability, the contracted elliptical cores become again linear in the limit where $c_{\perp 1}/c_{\parallel} \ll 1$, such that π also provides some upper bound for ϕ_{piv} in this limit. For $c_{\perp 1}/c_{\parallel}$ in between 1/2 and 1/3, as is the case here, ϕ_{piv} should be some fraction of π less than one. This is consistent with the saturation of $\Delta\phi^{\max}$ around $\approx 100^\circ - 120^\circ$ in Fig. 9.

The peak amplitude of twist along the filament, W^{\max} , can be much larger than $\Delta\phi^{\max}/S$ because twist is spatially localized. We can estimate W^{\max} to be the change of angle across a twiston, or, approximately, ϕ_{piv} , divided by its width l . We observe that $l \sim 2$ mm, which is larger but comparable to the width ξ of the excitation wavefront that is the smallest natural length scale in the problem. This yields the estimate $W^{\max} \sim \phi_{piv}/l$. For $\phi_{piv} \approx \pi$ and $\xi \approx 2$ mm, W^{\max} is about $100^\circ/\text{mm}$ which is about twice larger than the maximum amplitude of $\sim 50^\circ/\text{mm}$ deduced from Fig. 14. This is because ϕ_{piv} is only about 100° (rather than 180°) for this case. However, this is the correct order of magnitude of intramural twist.

3. Vortex multiplication and VF

The present results pinpoint specific mechanisms by which twist leads to the creation of additional vortex lines. The two dominant mechanisms that we have observed are shown schematically in Fig. 21. The first one (a) is the collision of a twist-generated curved section of the original transmural line with one surface as shown in Fig. 12. Extending the vortex line through the boundary, this corresponds to pinching-off a closed ring from this line. The second mechanism (b) is the expansion of a twisted half-ring intramurally that then collides with the opposite boundary to form two separate transmural lines, as shown in the first few frames of Fig. 16. Existing analytical theories predict that twist decouples from filament motion³⁹ and that vortex rings shrink for normal excitability. This prediction, however, is

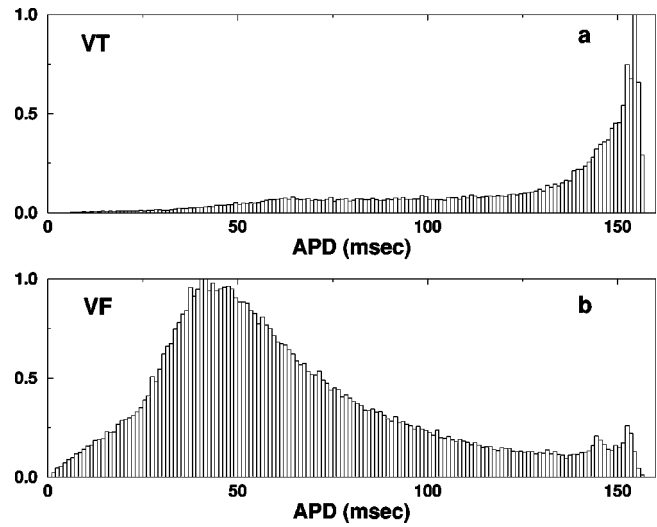


FIG. 19. Histograms of APD, measured at a voltage threshold of -60 mV, obtained from 4800 simultaneous recordings sites equally distributed on three square meshes of edge 0.155 cm on the endocardium, midwall, and epicardium for 3.5 s of run time: (a) VT, and (b) VF, for the same parameters as in Fig. 18. The bin height is normalized to be the number of APDs that fall within a given bin of 1 msec width divided by the highest number of APDs in bins.

only valid for a slowly varying twist along a vortex line in an isotropic medium and need not apply here. Actually our results suggest that a large twist renders the tension of the instantaneous vortex line negative, causing rings to expand.

Although mechanisms (a) and (b) above dominate during the initial decay into VF, other topological changes play

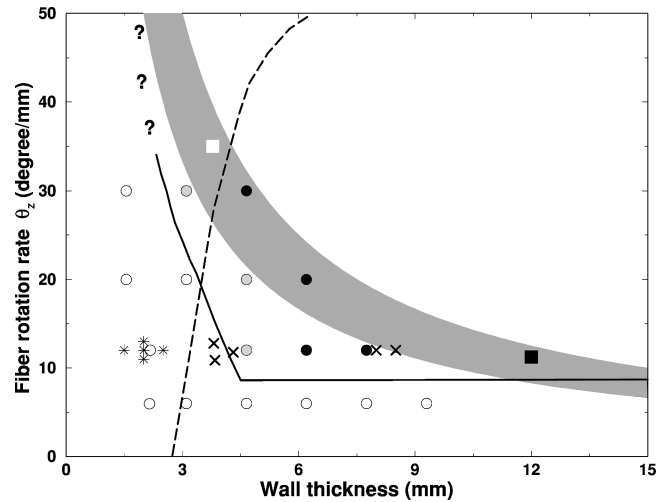


FIG. 20. Summary of simulation results in the plane of wall thickness and fiber rotation rate. Three regimes are distinguished: VT (open circles); intermediate VT-VF state (gray circles); and developed VF (solid circles). Results of the experiments of Kavanagh *et al.* (Ref. 31) are superimposed showing stable VT (stars) and VF (crosses), as well as those of Zipes *et al.* (Ref. 30) showing VT and VF in canine RV (open square) and LV (solid square), respectively. The shaded area is comprised between the curves $\theta_z = \Delta\theta/S$ for $\Delta\theta = 100^\circ$ and 150° . The dashed line is the nearly vertical boundary between VT and VF, conjectured by Winfree in Ref. 33. The solid line is the boundary inferred from our simulations. The lower horizontal part of this boundary moves up when lowering uniformly the excitability of the tissue since the minimum fiber rotation rate necessary to produce a large amplitude twist and filament distortion is increased.

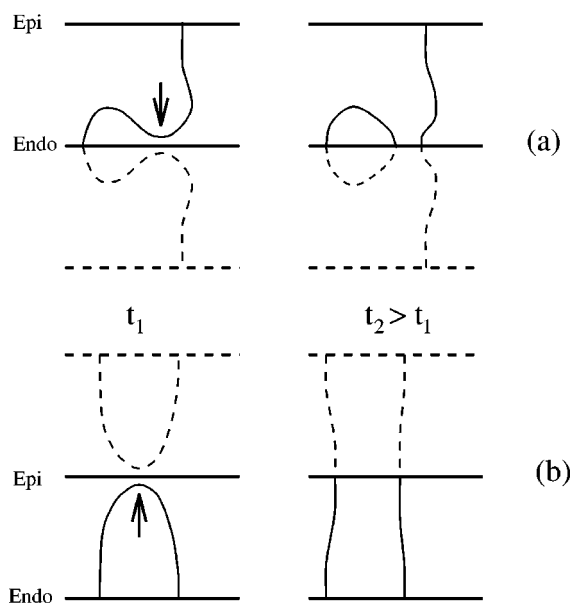


FIG. 21. Schematic representation of the dominant mechanisms of filament creation during the initial decay into VF by either: (a) collision with the boundary of a curved section of the original transverse vortex line following instability and the propagation of a twist; and (b) the expansion of a twisted half-ring. The dashed lines indicate mirror images through the boundaries. In developed VF vortex rings are also spontaneously created intramurally or on boundaries.

an important role in the fully developed turbulent state. For example, for large $S \sim 1$ cm, formation of a closed intramural ring can occur by pinching of the vortex line near the mid-wall, without collision. Transmural lines can coalesce to form half-rings on opposite surfaces. Furthermore, rings can form spontaneously by conduction blocks, either intramurally or manifested as half-rings ending on surfaces. These rings, however, are usually short lived and shrink and disappear on a time scale much shorter than the period, unless highly twisted. The fact that rings form at all intramurally indicates that the minimum wall thickness for their formation is not one spiral core diameter (which is ≈ 3 cm here and obviously larger than the wall thicknesses simulated here.) A better estimate of this minimum thickness is probably the diameter of one of the small outward petal, which is about the minimum size required for a brief pivot of the activation wavefront.

We expect these mechanisms should be universally present for high membrane excitability. They occur in simulation of the other model fits discussed in Sec. IV and hence do not require specific forms of APD restitution curves. This is what one would intuitively expect since winding of the filament only requires rapid pivot turns of the wavefront in-between arcs, a structure which is already present for a flat restitution curve. The MLR-I and GP parameters with apparently more realistic linear cores than MBR also exhibit a transition to VF above a comparable thickness than MBR.

We have found that reducing the membrane excitability has a stabilizing effect. For $\bar{g}_{fi}=4$ decay occurs for S larger than about 4–6 mm, whereas for $\bar{g}_{fi}=2.47$, it does not occur up to $S=1$ cm. In both cases, twist is sufficient to induce a morphological instability of the filament for S larger than

about 5 mm. Also, in both cases, twistons are observed and mechanism (a) in Fig. 21 leads to the formation of a half-ring vortex line on the opposite surface of where the filament is wound. However, for the reduced excitability, the half-ring shrinks and vanishes until the process is again repeated. Therefore the dynamics remains dominated by a single transmural line, whereas for $\bar{g}_{fi}=4$ the half-ring expands thereby leading to the creation of additional lines by mechanism (b). One possible explanation for this difference is that ϕ_{piv} is smaller for the tight turns on the elliptical-like trajectories than for the turns on small outward petals. Consequently reducing the excitability also tends to reduce the twist amplitude and may prevent further decay into VF.

The present results seem consistent with the current belief that uniform (i.e., spatially homogeneous) depression of excitability makes the heart less vulnerable to VF, which is the intended role of class I anti-arrhythmic drugs. This belief, however, may not be entirely correct since reducing excitability has also been shown to facilitate the induction of reentry by anatomical obstacles.⁸⁷ So, if the present mechanism of turbulence turns out to be relevant, designing anti-arrhythmic drugs may require careful dosage since both high and low excitability seem dangerous. The “safe” range of excitability, if existent, may be quite narrow.

B. Comparison with previous works and other three-dimensional mechanisms of VF

Sproing^{40,42} and the present instability are both induced by an excess of twist. However, they are manifested in fundamentally different ways. During sproing, as discovered numerically by Henze *et al.*,⁴⁰ the vortex line evolves into a *static* helical configuration. In contrast, during the present instability, a localized twist-induced distortion is *propagated* along the filament. In the former case twist is redistributed uniformly along the filament, whereas in the latter case it is predominantly carried with the disturbance and “dumped” at boundaries. This propagative character of the instability, which is absent from sproing, has to our best knowledge no previous analog in excitable media.

If the filament distortion carried by twistons were helical, this would indicate that the present instability is related to sproing. However, so far, our attempts to visualize three-dimensionally the filament did not show a simple helical distortion. Moreover, sproing develops in about one rotor period, whereas the filament distortion associated with a twiston is created in a much shorter time than one period. One could argue that one should compare instead one rotor period in Henze *et al.*’s simulations to one rotation around a small outward petal here, during which winding occurs. In this case the time scales for the two instabilities are comparable. Measuring torsion simultaneously with twist in our simulations should shine more light on the relation, if any, between the present instability and sproing.

Propagation failure is not observed here in the initial instability. One can see from Fig. 8(a)–(c) that the rotor period remains almost constant (≈ 160 ms) as S is increased. The excitable gap is the same here as in Beeler-Reuter, and thus small, but is not wound out by twist as observed in a

chemical medium.⁴¹ This is simply because twist is periodically relaxed and does not build-up on the time scale of the rotor period.

In the simulation of Panfilov and Keener,²⁸ destabilization of reentry by rotational anisotropy was interpreted to be caused by wave breaks tied to discrete effects of myocardium, also argued previously by Keener to be important.^{88,89} Their simulation therefore mixes two effects: anisotropic propagation (different propagation velocity parallel and perpendicular to the fiber), which would be present in continuous tissue, and anisotropic refractoriness (different refractory periods parallel and perpendicular to the fiber). The latter effect is absent here, making a qualitative comparison difficult. However the present instability mechanism appears to be different since wave breaks are absent initially.

In a 3D simulation without rotational anisotropy, Panfilov and Hogeweg⁹⁰ found three-dimensional scroll breakup in a modified FN model that already generates spiral wave breakup in 2D.⁹⁰ In this case, the decay into wave turbulence has its origin in a plane wave instability under high frequency forcing as in Ref. 54. The main role of the third dimension is to enlarge slightly the range of parameters for breakup as compared to 2D. In contrast here, with rotational anisotropy, the third dimension becomes essential to produce VF in a parameter range where VT is quite stable in 2D.

In a simulation study of FN kinetics, also without rotational anisotropy, Biktashev *et al.*³⁹ have proposed that filament tension could provide a 3D mechanism for VF. The filament tension is the coefficient γ in the equation of motion $dR/dt = -\gamma/R$ of the core of a scroll ring of radius R . The ring either shrinks if $\gamma > 0$ or expands if $\gamma < 0$. Furthermore, for $\gamma < 0$, small sinusoidal perturbations of wave vector q (i.e., of wavelength $2\pi/q$) of an initially straight filament grow in amplitude exponentially in time as $\sim \exp(\Omega t)$, where $\Omega \sim -\gamma q^2$ for small q . So small perturbations grow for $\gamma < 0$ and decay for $\gamma > 0$. Biktashev *et al.*³⁹ observe numerically that this causes the filament to curve and hit the boundaries causing new filaments to be created. The main difference is that the vortex line instability is generated here by twist for normal membrane excitability, whereas, with negative tension, it develops without twist for a reduced excitability.

For the range of excitability of Fig. 7, we find numerically that γ is positive in the normal excitability linear-core regime and negative in the reduced excitability inward petal/circular-core regime, according to expectation. Furthermore, we find that for a filament instability to develop on a time scale of a few rotor periods, S needs to be larger than about two to three times r_c . Examination of Fig. 7 leads to the conclusion that this negative core tension mechanism is not relevant here for $S \leq 2$ cm.

C. Comparison with experiment and possible tests

Figure 20 reproduces Fig. 1 of Winfree in Ref. 33 with our simulations results superimposed for the purpose of comparison with experiment. Simulations results have been plot-

ted by distinguishing between VT (open circles), intermediate VT-VF (shaded circles), and developed VF (filled circles).

The nearly vertical dashed line represents Winfree's putative guess of the VT-VF boundary that interpolates between the RV-LV experiment of Zipes *et al.*³⁰ and the LV wall thinning experiment of Kavanagh *et al.*³¹ As such, this boundary implies that fiber rotation has an almost neutral role, perhaps even stabilizing if we interpret the slight bend to the right of this boundary as significant. The solid line in Fig. 20 represents the boundary between VT and VF interpolated between our simulation results for normal excitability. This boundary shows that fiber rotation has a destabilizing role for two reasons. First, it shows that there exists a minimum θ_z , corresponding to the approximately horizontal lower part of the boundary, below which turbulence is absent for any S . Second, it shows that the transition to turbulence occurs at smaller S for increasing θ_z above this minimum, as reflected by the fact that the nearly vertical part of the boundary bends to the left for larger θ_z . Also, the lower horizontal part must move up with lowering excitability since we do not observe turbulence for a smaller \bar{g}_{Na} . So the picture to emerge is that two conditions need to be simultaneously met to obtain turbulence. First, a minimum fiber rotation rate, which increases with decreasing excitability, is needed to produce a sufficiently large twist to cause a large filament disturbance. Second, a minimum wall thickness, which is only weakly dependent on fiber rotation rate, is necessary for this disturbance to develop sufficiently to create new filaments by collision.

In the simulations, the transition from VT to VF occurs in the range of 4–6 mm for $\theta_z = 12^\circ/\text{mm}$. This is about the thickness at which the transmural twist angle reaches its peak amplitude $\sim \pi/S$ (for this θ_z) and where there is sufficient room intramurally for curved sections of filaments to cause the creation of new vortices by collision at boundaries. This critical thickness is consistent with the one observed experimentally for the LV. For $\theta_z = 30^\circ/\text{mm}$, the transition occurs in the range of 2–4 mm so a 4-mm RV is marginally unstable. However, we have not yet scanned sufficiently the upper left-hand corner of Fig. 20 to conclude if a thinner RV would fibrillate.

Can one conceive of experimental tests of the present instability? To our knowledge, only one experiment to date⁹¹ has attempted to map different layers and reported no noticeable twist. However this was for the RV and an angle of fiber rotation of apparently only $\approx 30^\circ$, judging from Fig. 9 in Ref. 91. It should also be possible to measure oscillations of the transmural twist angle in a VT regime, such as those shown in Fig. 8. This would require to map the endocardium (with the Purkinje fiber removed) and epicardium simultaneously for the LV or RV or thinner sections of those. It would also necessitate to record this activity with sufficient time resolution to capture these oscillations and, more importantly, to image the activation wavefronts on each layer with sufficient spatial resolution to extrapolate the orientation of the wavefront at the point of phase singularity.

Furthermore, the existence of twistons and the related mechanism by which vortices are created could be detected

by timing events on the epicardium and endocardium. This is clearly illustrated in Fig. 13, which shows the voltage activity on the epicardium and endocardium associated with the creation and transmural propagation of a twiston corresponding to Fig. 12. In the first few frames of this example, one can see that the wavefront pivots rapidly on the epicardium before the endocardium. This signals that a twiston should be created below the epicardium and propagate transmurally in a time $\sim S/c_{\perp 2}$. One should therefore expect a breakthrough of activation on the endocardium after about this delay time. Since twistons can also propagate from the endocardium to the epicardium, identical breakthrough events should also be observable on the epicardium that is easier to map experimentally. These events should have generally two stages: the first, appearance of a growing target pattern as a curved section of intramural filament approaches the surface, and then the subsequent creation of two additional point of phase singularities corresponding to the collision.

Lastly, the transmembrane recordings of Fig. 18 show that there is considerably more variability in the signal measured at a single point during VT than VF. Moreover, we have shown that there is a clear correlation between the filament density and the histogram distribution of APD shown in Fig. 19. This distribution becomes broader and shifts to small APD during VF because the passage of a vortex line near a recording site leads to a short APD. So APD distributions should provide a useful means to characterize the vortex density during VF in addition to the other methods that have been proposed.⁴⁷

D. Limitations and prospects

A number of limitations of the present study should be mentioned. First, we have assumed that, aside from rotational anisotropy, the tissue is homogeneous (i.e., I_{ion} is the same for all cells). VF has been historically hypothesized to be caused by random variations of pulse durations, or so-called dispersion of refractoriness. The pioneering cellular automata simulations of Moe *et al.*⁹² and others since,⁹³ have clearly demonstrated that such random variations trigger wavebreaks. However dispersion of refractoriness produces VF in both 2D and 3D, which does not seem consistent with the data. More importantly, modern optical mapping techniques show that spatial variations of refractoriness are not random, as hypothesized in these models, but spatially graded.⁹⁴ Gradients of refractoriness typically produce vortex drift but not wave breakup. Thus it would be desirable in the future to include such gradient effects. Our expectation is that this drift should not change the main mechanism of vortex creation since twistons are produced on a sufficiently short time scale by the proposed leading pivot turn mechanism. We have neglected macroscopic inhomogeneities that have been shown for example to anchor filaments.⁹⁵ Such a type of defect may also reduce the amount of twist build-up by providing intramural unwinding surfaces. However, such inhomogeneities would probably need to be on a mm scale comparable to the width of twistons to halt their propagation, which seems large.

Second, we have used a simplified ionic model of elec-

trical activity rather than modified forms of the original Beeler-Reuter equation or more up to date models that may produce stable reentry in 2D. Future work may be required to ensure that we have not lost essential features, or introduced spurious ones, by this simplification. However, we do not expect that this is the case since the present model produces the main features of 2D re-entry exhibited by the more complex models.

Lastly, we have focused on a fairly specific class of initial conditions and an idealized geometry. It would be desirable to extend the present simulations to a geometry more representative of the whole ventricle and initiate reentry by a premature stimulus.

IX. CONCLUSIONS

We have presented a simplified three-variable ionic model that approximates well the behavior of more complex ionic models such as Beeler-Reuter, and an efficient numerical algorithm to simulate this model in a rotationally anisotropic continuous tissue.

Winfree conjectured previously³³ that some vortex filament instability should be present to explain the fact that only thick enough hearts tend to fibrillate, but left the mechanism of this instability unspecified. Our simulations pinpoint a specific instability mechanism induced by fiber rotation.⁸⁴

This instability is distinct from sproing⁴⁰ in that it is manifested by the propagation of localized twist-induced distortions of the filament, rather than a static helicoidal deformation. It involves a winding mechanism that produces a large twist amplitude and a strong coupling between twist and filament motion that produces the distortion. Winding occurs by rapid pivoting by an angle $\phi_{\text{piv}} \sim 100^\circ - 200^\circ$ of the wavefront on one bounding surface that leads in time the pivot turn of the wavefront on the opposite surface. This produces transmural twist amplitudes $\Delta\phi \sim \phi_{\text{piv}}/S$, local peak amplitudes along the filament of $W^{\text{max}} \sim \phi_{\text{piv}}/l$, where l is the width of twistons, and a build-up of twist on a time scale of $t_{\text{piv}} \sim 10 - 20$ ms. The smallness of this time scale accounts for why the twist amplitude starts to rise at surprisingly small S (of about 1 mm), and why twist cannot simply decay diffusively in the larger S regime where twistons are created. The rapid pivot turns occur twice per rotor period during meander along arcs of conduction blocks, which is characteristic of reentry in a regime of normal excitability. Consequently, the vortex line also becomes unstable twice per period, the instability lasting only for a short time $\sim S/c_{\perp 2}$ that is about the time for a twiston to propagate transmurally.

The mechanism by which this instability leads to VF differs from other known instabilities and turbulence mechanisms reviewed here. It involves rotational anisotropy in a simple continuum but not wave breaks produced by discrete effects.²⁸ It does not depend on underlying plane wave instabilities that already produce 2D turbulence, patchy failure induced by a twist gradient, and is not based on a negative core filament tension characteristic of a reduced excitability. Moreover, it does not involve dispersion of refractoriness still often viewed as the main cause of VF. New vortices are

initially created instead by surface collisions of distorted unstable filaments. Furthermore, we have argued that specific experimental signatures of this mechanism should be observable by simultaneously mapping the epicardium and endocardium, and timing events on these surfaces. The time to decay into VF is roughly the time to create enough filaments to reach some maximum average packing of vortices, or a few rotor periods, and the presence of a high filament density broadens the APD distribution and shifts its maximum to shorter time.

Rotational anisotropy is rendering vortex dynamics already much richer than one may have expected in idealized homogeneous and continuous tissue. We have only qualitatively interpreted here some numerical observations and we do not yet have theories to describe the coupling of highly localized twist excitations to filament motion in such a nonlinear regime. We do not know how to predict the thickness at which VT should decay into VF as a function of fiber rotation rate and other parameters of the medium, and how this decay may be altered by different initial conditions. Moreover, many anatomical features can cause the heart to depart from an idealized continuum, and it is not clear how those will modify this rich behavior, either simplifying it or making it more complicated.

ACKNOWLEDGMENTS

This research is supported by the American Heart Association.

APPENDIX A

In this Appendix, we describe how the algorithm of Sec. III can be extended to the case of anisotropic propagation with $I_{\text{ion}} \neq 0$. We restrict our attention to Eqs. (24)–(26) of the three-current model and denote J_{ion} simply by J for brevity of notation. This algorithm is applicable to more general ionic models with one restriction on the sodium kinetics that is emphasized below.

The first operator O_1 is now chosen to include all spatial derivatives in the x - y plane as well as the current term J . The second operator O_2 is the same as before and only involves diffusion along z . For stepping O_1 , the membrane potential that enters in J is treated implicitly by linearization. This corresponds to approximating J during this step by

$$\frac{1}{2} [J(u_\alpha^S; \mathbf{y}_\alpha^n) + J(u_\alpha^n; \mathbf{y}_\alpha^n)] = J_\alpha^n + \frac{1}{2} J_{u_\alpha}^n (u_\alpha^S - u_\alpha^n) + \dots, \quad (\text{A1})$$

where we have defined $J_\alpha^n \equiv J(u_\alpha^S; \mathbf{y}_\alpha^n)$, and $J_{u_\alpha}^n \equiv \partial_{u_\alpha} J(u; \mathbf{y})$, evaluated at $u = u_\alpha^n$ and $\mathbf{y} = \mathbf{y}_\alpha^n$. This implicit treatment is needed because of the rapid upstroke of the action potential on the time scale $\tau_d \sim C_m / \bar{g}_{\text{fi}}$, where \bar{g}_{fi} is the maximum sodium conductance. In contrast, the gate variables v and w can be simply treated explicitly because of their slower kinetics (i.e., because τ_v^\pm and τ_w^\pm are larger than τ_d). In ionic models such as BR and LR, the gate variables \mathbf{y} also generally vary on time scales larger than τ_d and do not need to be treated implicitly. One exception to this rule is the gate m responsible for activation of the Na current of the form $I_{\text{Na}} = m^3 h j(V - V_{\text{Na}})$. This gate varies on a time scale much shorter than τ_d and severely constrains Δt . This problem does not arise in the simplified ionic model because the form of I_{Na} for this model is equivalent to adiabatically eliminating m by letting $m = m_\infty(u)$. The present algorithm would therefore only be advantageous for ionic models where gate variables substantially faster than τ_d are either adiabatically eliminated, or integrated separately with a smaller time step using operator splitting.

Next, the partial derivative $\delta_{xy}^2 u_\alpha^n$ associated with fiber rotation is treated explicitly using a second order Adams–Bashforth scheme. This, together with the implicit treatment of J , leads to the algorithm defined by the sequence of implicit steps

$$\left. \begin{aligned} u_\alpha^S &= u_\alpha^n + \beta_x \delta_x^2 u_\alpha^S + \beta_y \delta_y^2 u_\alpha^n + 2\beta_{xy} \left(\frac{3}{2} \delta_{xy}^2 u_\alpha^n - \frac{1}{2} \delta_{xy}^2 u_\alpha^{n-1} \right) - \Delta t J_\alpha^n - \frac{\Delta t}{2} J_{u_\alpha}^n (u_\alpha^S - u_\alpha^n) \\ u_\alpha^{n+1} &= u_\alpha^S + \frac{\beta_z}{2} (\delta_z^2 u_\alpha^{n+1} + \delta_z^2 u_\alpha^S) \end{aligned} \right\} \quad n \text{ even} \quad (\text{A2})$$

$$\left. \begin{aligned} u_\alpha^S &= u_\alpha^n + \beta_x \delta_x^2 u_\alpha^n + \beta_y \delta_y^2 u_\alpha^S + 2\beta_{xy} \left(\frac{3}{2} \delta_{xy}^2 u_\alpha^n - \frac{1}{2} \delta_{xy}^2 u_\alpha^{n-1} \right) - \Delta t J_\alpha^n - \frac{\Delta t}{2} J_{u_\alpha}^n (u_\alpha^S - u_\alpha^n) \\ u_\alpha^{n+1} &= u_\alpha^S + \frac{\beta_z}{2} (\delta_z^2 u_\alpha^{n+1} + \delta_z^2 u_\alpha^S) \end{aligned} \right\} \quad n \text{ odd}, \quad (\text{A3})$$

where we have defined the constants $\beta_x = D_{\parallel} \Delta t / \Delta^2$, $\beta_y = D_{\perp 1} \Delta t / \Delta^2$, $\beta_z = D_{\perp 2} \Delta t / \Delta z^2$, and $\beta_{xy} = D_{12} \Delta t / \Delta^2$. As before, the n even and odd steps are identical except for the interchange of x and y that corresponds to alternatively stepping x and y implicitly every two time steps. The stepping of the gate variables can be done efficiently by noting that the

dynamics of v and w defined by Eqs. (25)–(26) can be integrated exactly from time $n\Delta t$ to time $(n+1)\Delta t$, which gives

$$\left. \begin{aligned} y_\alpha^{n+1} &= y_\alpha^n e^{-\Delta t / \tau_y^+}, \quad \text{for } u > u_c \\ y_\alpha^{n+1} &= 1 - [1 - y_\alpha^n] e^{-\Delta t / \tau_y^-}, \quad \text{for } u < u_c \end{aligned} \right\} \quad n \text{ even or odd} \quad (\text{A4})$$

for $y=(v,w)$. We note that this simplification is only possible because of the simplified form assumed for the dynamics of the gate variables. For more general models, the gate variables can be time stepped explicitly (with the aforementioned caveat for m) using an Euler scheme or a second order Adams–Bashforth scheme.

APPENDIX B

As described in Sec. VI, we define the filament by the line (or set of lines if more than one filament is present) of intersection of the two surfaces $V(\mathbf{r},t)=V_{\text{iso}}$, where V_{iso} is some arbitrary threshold potential used to distinguish polarized and depolarized regions of the tissue, and $\partial_t V(\mathbf{r},t)=0$. In a simulation where time is discrete, we can approximate $\partial_t V(\mathbf{r},t) \approx [V(\mathbf{r},(n+1)\Delta t) - V(\mathbf{r},n\Delta t)]/\Delta t$. The task of determining the filament position is then reduced to finding the line of intersection of the two surfaces defined by

$$V(\mathbf{r},n\Delta t) = V(\mathbf{r},(n+1)\Delta t) = V_{\text{iso}}. \quad (\text{B1})$$

As a practical matter, it is convenient to represent this line by the set of intersection points, denoted by $\mathbf{R}_1, \mathbf{R}_2, \dots$, of this line with the lattice planes defined by $x=i\Delta$, $y=j\Delta$, and $z=k\Delta$ (which are just all the y - z , x - z , and x - y planes that contain lattice points, respectively.) Since each plane is made up of squares of edge Δ , with one lattice point at each of the four corners, the algorithm proceeds by finding which of the $3N_x N_y N_z$ squares contained in these planes are intersected by the line defined by Eq. (B1) and what are the coordinates of these intersection. To illustrate how to this is done, let us consider for example the square in the $z=k\Delta$ plane defined by the four lattice points $V_{i,j,k}^n$, $V_{i+1,j,k}^n$, $V_{i,j+1,k}^n$, and $V_{i+1,j+1,k}^n$ (the generalization to other squares is then trivial by symmetry). We define the scaled orthogonal coordinates $\bar{x}=(x-i\Delta)/\Delta$ and $\bar{y}=(y-j\Delta)/\Delta$ that vary between 0 and 1 inside this square. To find the point of intersection of the line defined by Eq. (B1) with this square, we simply approximate $V(\mathbf{r},n\Delta t)$ and $V(\mathbf{r},(n+1)\Delta t)$ inside this square by a bilinear interpolation formula. We then impose the condition of Eq. (B1), which yields the set of two simultaneous equations:

$$(1-\bar{x})(1-\bar{y})V_{i,j,k}^n + \bar{x}(1-\bar{y})V_{i+1,j,k}^n + \bar{x}\bar{y}V_{i+1,j+1,k}^n + (1-\bar{x})\bar{y}V_{i,j+1,k}^n = V_{\text{iso}}, \quad (\text{B2})$$

$$(1-\bar{x})(1-\bar{y})V_{i,j,k}^{n+1} + \bar{x}(1-\bar{y})V_{i+1,j,k}^{n+1} + \bar{x}\bar{y}V_{i+1,j+1,k}^{n+1} + (1-\bar{x})\bar{y}V_{i,j+1,k}^{n+1} = V_{\text{iso}}, \quad (\text{B3})$$

for the two unknowns \bar{x} and \bar{y} . Then, if Eqs. (B2) and (B3) have a solution with $0 \leq \bar{x} \leq 1$ and $0 \leq \bar{y} \leq 1$, there exists an intersection of the filament with this square. This intersection corresponds in this particular example to the vector $\mathbf{R}_l = (i+\bar{x})\Delta\mathbf{x} + (j+\bar{y})\Delta\mathbf{y} + k\Delta\mathbf{z}$. Points of intersections with all squares are then determined by a similar procedure. Finally, all of these points are sorted in order of increasing arclength s along a given filament, the arclength distance between two nearby points being simply defined by the Euclidean distance $\Delta s_l = |\mathbf{R}_{l+1} - \mathbf{R}_l|$. The total length of this filament is then given by $L = \sum_{j=1}^N \Delta s_j$, where N is the total number of points along the filament.

To calculate twist we need to calculate the components of the vector $\mathbf{N} = \nabla V / |\nabla V|$ at each point \mathbf{R}_l along the filament. This is done by first calculating these components on lattice points with finite difference formulae, and then using the same bilinear interpolation formulae as above to calculate them at the intersection points of the filament. Next, we calculate the components of the unit vector $\mathbf{t}_l \equiv (\mathbf{R}_{l+1} - \mathbf{R}_l) / |\mathbf{R}_{l+1} - \mathbf{R}_l|$ that joins two nearby points along the filament. We then evaluate the angle $\Delta\phi_l$ between \mathbf{N}_l and the projection of \mathbf{N}_{l+1} in the plane spanned by \mathbf{N}_l and the binormal $\mathbf{t}_l \times \mathbf{N}_l$, or

$$\Delta\phi_l = (\mathbf{N}_{l+1} \times \mathbf{N}_l) \cdot \mathbf{t}_l. \quad (\text{B4})$$

This allows us to construct the function $\phi(s)$, or $\phi_l = \sum_{j=1}^l \Delta\phi_j$, whose derivative $W(s) = \partial_s \phi(s)$ is the twist. This derivative is smoothed out by interpolating the function $\phi(s)$ between points (\mathbf{R}_l) along the filament with cubic splines.

¹A. T. Winfree, *When Time Breaks Down* (Princeton University Press, Princeton, NJ, 1987).

²V. Zykov, *Simulation of Wave Processes in Excitable Media* (Nuaka, Moscow, 1984).

³R. Gray and J. Jalife, "Spiral waves and the heart," *Int. J. Bifurcation Chaos Appl. Sci. Eng.* **6**, 415 (1996).

⁴V. Krinsky and A. Pumir, "Models of defibrillation in cardiac tissue," *Chaos* **8**, 188–203 (1998).

⁵V. Biktashev and A. Holden, "Re-entrant waves and their elimination in a model of mammalian ventricular tissue," *Chaos* **8**, 48–56 (1998).

⁶F. Witkowski *et al.*, "A method for visualization of ventricular fibrillation: Design of a cooled fiber optically coupled image intensified CCD data acquisition system incorporating wavelet shrinkage based adaptive filtering," *Chaos* **8**, 94–102 (1998).

⁷J. Davidenko *et al.*, "Stationary and drifting spiral waves of excitation in isolated cardiac muscle," *Nature (London)* **355**, 349 (1992).

⁸R. Gray *et al.*, "Nonstationary vortexlike reentrant activity as a mechanism of polymorphic ventricular tachycardia in the isolated rabbit heart," *Circulation* **91**, 2454 (1995).

⁹P. Bayly *et al.*, "A quantitative measurement of spatial order in ventricular fibrillation," *J. Cardiovasc. Electrophysiol.* **4**, 533 (1993).

¹⁰A. Garfinkel *et al.*, "Quasiperiodicity and chaos in cardiac fibrillation," *J. Clin. Invest.* **99**, 1 (1997).

¹¹D. Noble, "A modification of the Hodgkin-Huxley equations applicable to Purkinje fibre action and pace-maker potentials," *J. Physiol. (London)* **160**, 317 (1962).

¹²G. Beeler and H. Reuter, "Reconstruction of the action potential of ventricular myocardial fibres," *J. Physiol. (London)* **268**, 177 (1977).

¹³D. D. Francesco and D. Noble, "A model of cardiac electrical activity incorporating ionic pumps and concentration changes," *Philos. Trans. R. Soc. London, Ser. B* **307**, 353 (1985).

¹⁴C. Luo and Y. Rudy, "A model of the ventricular cardiac action potential," *Circ. Res.* **68**, 1501 (1991).

¹⁵C. Luo and Y. Rudy, "A dynamic model of the cardiac ventricular action potential I. Simulations of ionic currents and concentration changes," *Circ. Res.* **74**, 1071 (1994).

¹⁶C. Henriquez and A. Papazoglou, "Using computer models to understand the roles of tissue structure and membrane dynamics in arrhythmogenesis," *Proc. IEEE* **84**, 334 (1996).

¹⁷M. Boyett and B. Jewell, "A study of the factors responsible for rate-dependent shortening of the action potential in mammalian ventricular muscle," *J. Physiol. (London)* **285**, 359 (1978).

¹⁸V. Elharrar and B. Surawicz, "Cycle length effect on restitution of action potential duration in dog cardiac fibers," *Am. J. Physiol.* **244**, H782 (1983).

¹⁹S. Girouard *et al.*, "Optical mapping in a new guinea pig model of ventricular tachycardia reveals mechanisms for multiple wavelengths in a single reentrant circuit," *Circulation* **93**, 603 (1996).

²⁰C. Thomas, "The muscular architecture of the ventricles of hog and dog hearts," *Am. J. Anat.* **101**, 17 (1957).

- ²¹ D. Streeter, "Gross morphology and fiber geometry in the heart," in *Handbook of Physiology*, edited by R. Berne (American Physiological Society, Bethesda, MD, 1979), Vol. 1, Section 2, pp. 61–112.
- ²² P. Nielsen, I. L. Grice, and B. Smaill, "Mathematical model of geometry and fibrous structure of the heart," *Am. J. Physiol.* **260**, H1365 (1991).
- ²³ C. Peskin, "Fiber architecture of the left ventricular wall: An asymptotic analysis," *Commun. Pure Appl. Math.* **42**, 79 (1989).
- ²⁴ J. Keener, "An eikonal-curvature equation for action potential propagation in myocardium," *J. Math. Biol.* **29**, 629 (1991).
- ²⁵ P. Franzzone, L. Guerri, and B. Taccardi, "Spread of excitation in a myocardial volume," *J. Cardiovasc. Electrophysiol.* **4**, 144 (1993).
- ²⁶ B. Taccardi, E. Macchi, and Y. Vyhmeister, "Effect of myocardial fiber direction on epicardial potentials," *Circulation* **90**, 3076 (1994).
- ²⁷ A. Pollard, M. Burgess, and K. Spitzer, "Computer simulations of three-dimensional propagation in ventricular myocardium. Effects of intramural fiber rotation and inhomogeneous conductivity on epicardial activation," *Circ. Res.* **72**, 744 (1993).
- ²⁸ A. Panfilov and J. Keener, "Re-entry in three-dimensional FitzHugh-Nagumo medium with rotational anisotropy," *Physica D* **84**, 545 (1995).
- ²⁹ D. Zipes, "Circulation," "Electrophysiological mechanisms involved in ventricular fibrillation," *Suppl. III* **51**, 120 (1975).
- ³⁰ D. Zipes *et al.*, "Termination of ventricular fibrillation in dogs by depolarizing a critical amount of myocardium," *Am. J. Cardiol.* **36**, 37 (1975).
- ³¹ K. Kavanagh *et al.*, "High-current stimuli to the spared epicardium of a large infarct induce ventricular tachycardia," *Circulation* **85**, 680 (1992).
- ³² A. Winfree, "Rotors, fibrillation, and dimensionality," in *Computational Biology of the Heart*, edited by A. Panfilov and A. Holden (Wiley, New York, 1997), pp. 101–135.
- ³³ A. Winfree, "Electrical turbulence in three-dimensional heart muscle," *Science* **266**, 1003 (1994).
- ³⁴ A. Winfree, "Stable particle-like solutions to the nonlinear wave equations of three-dimensional excitable media," *SIAM (Soc. Ind. Appl. Math.) Rev.* **32**, 1 (1990).
- ³⁵ A. Mikhailov, A. Panfilov, and A. Rudenko, "Twisted scroll waves in active three-dimensional media," *Phys. Lett. A* **109**, 246 (1985).
- ³⁶ J. Keener, "The dynamics of three-dimensional scroll waves in excitable media," *Physica D* **31**, 269 (1988).
- ³⁷ V. Biktashev, "Evolution of twist of an autowave vortex," *Physica D* **36**, 167 (1989).
- ³⁸ J. Keener and J. Tyson, "The dynamics of scroll waves in excitable media," *SIAM (Soc. Ind. Appl. Math.) Rev.* **34**, 1 (1992).
- ³⁹ V. Biktashev, A. Holden, and H. Zhang, "Tension of organizing filaments of scroll waves," *Philos. Trans. R. Soc. London, Ser. A* **347**, 611 (1994).
- ⁴⁰ C. Henze, E. Lugosi, and A. Winfree, "Helical organizing centers in excitable media," *Can. J. Phys.* **68**, 683 (1989).
- ⁴¹ A. Pertsov, R. Aliev, and V. Krinsky, "Three-dimensional twisted vortices in an excitable chemical medium," *Nature (London)* **345**, 419 (1990).
- ⁴² S. Mironov, M. Vinson, S. Mulvey, and A. Pertsov, "Destabilization of three-dimensional rotating chemical waves in an inhomogeneous BZ reaction," *J. Physiol. (London)* **100**, 1975 (1996).
- ⁴³ A. Winfree, "Estimating the ventricular fibrillation threshold," in *Theory of Heart*, edited by L. Glass, P. Hunter, and A. McCulloch (Springer-Verlag, New York, 1991), pp. 477–531.
- ⁴⁴ A. Winfree, "Evolving perspectives during 12 years of electric turbulence," *Chaos* **8**, 1–19 (1998).
- ⁴⁵ R. Gray *et al.*, "Mechanisms of cardiac fibrillation," *Science* **270**, 1222 (1995).
- ⁴⁶ J. Jalife, R. Gray, G. Morley, and J. Davidenko, "Self-organization and the dynamical nature of ventricular fibrillation," *Chaos* **8**, 79–93 (1998).
- ⁴⁷ P. Bayly *et al.*, "Spatial organization, predictability, and determinism in ventricular fibrillation," *Chaos* **8**, 103–115 (1998).
- ⁴⁸ A. Panfilov and A. Holden, "Spatiotemporal irregularity in a two-dimensional model of cardiac tissue," *Int. J. Bifurcation Chaos Appl. Sci. Eng.* **1**, 219 (1991).
- ⁴⁹ M. Courtemanche and A. Winfree, "Re-entrant rotating waves in a Beeler-Reuter based model of two-dimensional cardiac electrical activity," *Int. J. Bifurcation Chaos Appl. Sci. Eng.* **1**, 431 (1991).
- ⁵⁰ M. Courtemanche, "Complex spiral wave dynamics in a spatially distributed ionic model of cardiac electrical activity," *Chaos* **6**, 579 (1996).
- ⁵¹ J. Leon, F. Roberge, and A. Vinet, "Simulation of two-dimensional anisotropic cardiac reentry: Effects of the wavelength on the reentry characteristics," *Ann. Biomed. Eng.* **22**, 592 (1994).
- ⁵² A. Panfilov and P. Hogeweg, "Spiral breakup in a modified FitzHugh-Nagumo model," *Phys. Lett.* **176**, 295 (1993).
- ⁵³ A. Karma, "Spiral breakup in model equations of action potential propagation in cardiac tissue," *Phys. Rev. Lett.* **71**, 1103 (1993).
- ⁵⁴ A. Karma, "Electrical alternans and spiral wave breakup in cardiac tissue," *Chaos* **4**, 461 (1994).
- ⁵⁵ M. Janse, "Vulnerability to ventricular fibrillation," *Chaos* **8**, 149–156 (1998).
- ⁵⁶ W. Press, W. Vetterling, S. Teukolsky, and B. Flannery, *Numerical Recipes Second Edition* (Cambridge University Press, Cambridge, MA, 1992).
- ⁵⁷ R. FitzHugh, "Impulses and physiological states in theoretical models of nerve membrane," *Biophys. J.* **1**, 445 (1961).
- ⁵⁸ A. Winfree, "Varieties of spiral wave behavior: An experimentalist's approach to the theory of excitable media," *Chaos* **1**, 303 (1991).
- ⁵⁹ A. Panfilov and A. Pertsov, *Dokl. Akad. Nauk SSSR* **274**, 1500 (1984).
- ⁶⁰ B. Kogan *et al.*, "The simplified FitzHugh-Nagumo model with action potential duration restitution," *Physica D* **50**, 327 (1991).
- ⁶¹ B. Kogan, W. Karplus, and M. Karpoukhin, "A third-order action potential model for computer simulation of electrical wave propagation in cardiac tissue," in *Computer Simulation in Biomedicine*, edited by H. Power and R. Hart (Computational Mechanics, Boston, 1995), pp. 147–154.
- ⁶² J. Nolasco and R. Dahlen, "A graphic method for the study of alternation in cardiac action potentials," *J. Appl. Physiol.* **25**, 191 (1968).
- ⁶³ M. R. Guevara, G. Ward, A. Shrier, and L. Glass, "Electrical alternans and period doubling bifurcations," in *Computers in Cardiology* (IEEE, 1984), pp. 167–170.
- ⁶⁴ H. Ito and L. Glass, "Theory of reentrant excitation in a ring of cardiac tissue," *Physica D* **56**, 84 (1992).
- ⁶⁵ L. Frame and M. Simson, "Oscillations of conduction, action potential duration, and refractoriness," *Circulation* **78**, 1277 (1988).
- ⁶⁶ T. Lewis and M. R. Guevara, "Chaotic dynamics in an ionic model of the propagated cardiac action potential," *J. Theor. Biol.* **146**, 407 (1990).
- ⁶⁷ W. Quan and Y. Rudy, "Unidirectional block and reentry of cardiac excitation: A model study," *Circ. Res.* **66**, 367 (1990).
- ⁶⁸ M. Courtemanche, L. Glass, and J. Keener, "Instabilities of a propagating pulse in a ring of excitable media," *Phys. Rev. Lett.* **70**, 2182 (1993).
- ⁶⁹ A. Karma, H. Levine, and X. Zou, "Theory of pulse instabilities in electrophysiological models of excitable tissues," *Physica D* **73**, 113 (1994).
- ⁷⁰ J. Tyson and J. Keener, "Singular perturbation theory of traveling waves in excitable medium," *Physica D* **32**, 327 (1988).
- ⁷¹ R. G. Jr, N. Otani, and M. Watanabe, "Memory and complex dynamics in cardiac Purkinje fibers," *Am. J. Physiol.* **272**, H1826 (1997).
- ⁷² A. Karma and F. Fenton, "Simplified ionic models of cardiac action potential" (to be published).
- ⁷³ V. Krinsky, I. Efimov, and J. Jalife, "Vortices with linear cores in excitable media," *Proc. R. Soc. London, Ser. A* **437**, 645 (1992).
- ⁷⁴ V. Krinsky and I. Efimov, "Vortices with linear cores in mathematical models of excitable media," *Physica A* **188**, 55 (1992).
- ⁷⁵ I. Efimov, V. Krinsky, and J. Jalife, "Dynamics of rotating vortices in the Beeler-Reuter model of cardiac tissue," *Chaos Solitons Fractals* **5**, 513 (1995).
- ⁷⁶ F. Fenton, Ph.D. thesis, Northeastern University, Boston, MA 02115 (1998).
- ⁷⁷ V. Hakim and A. Karma, "Spiral wave meander in excitable media: The large core limit," *Phys. Rev. Lett.* **79**, 665 (1997).
- ⁷⁸ D. Barkley, "Euclidean symmetry and the dynamics of rotating spiral waves," *Phys. Rev. Lett.* **72**, 164 (1994).
- ⁷⁹ V. Biktashev, A. Holden, and E. Nikolaev, "Spiral wave meander and symmetry of the plane," *Int. J. Bifurcation Chaos Appl. Sci. Eng.* **6**, 2433 (1996).
- ⁸⁰ W. Jahnke, W. Skaggs, and A. Winfree, "Chemical vortex dynamics in the Belousov-Zhabotinsky reaction and in the two-variable Oregonator model," *J. Phys. Chem.* **93**, 740 (1989).
- ⁸¹ V. P. G. Li, Q. Ouyang, and H. Swinney, "Transition from simple rotating chemical spirals to meander and traveling spirals," *Phys. Rev. Lett.* **77**, 2105 (1996).
- ⁸² D. Kim *et al.*, "Electrical turbulence as a result of the critical curvature for propagation in cardiac tissue," *Chaos* **8**, 137–148 (1998).
- ⁸³ S. Dillon, P. Uersell, and A. Wit, "Pseudo-block caused by anisotropic conduction: A new mechanism for sustained reentry," *Circulation* **72**, 1116 (1985).
- ⁸⁴ F. Fenton and A. Karma, "Rotational-anisotropy-induced wave turbulence in thick myocardium" (to be published).
- ⁸⁵ H. Hasimoto, "A soliton on a vortex filament," *J. Fluid Mech.* **51**, 477 (1972).

- ⁸⁶E. Hopfinger, F. Browand, and Y. Gagne, "Turbulence and waves in a rotating tank," *J. Fluid Mech.* **125**, 505 (1982).
- ⁸⁷C. Cabo, A. Pertsov, J. Davidenko, and J. Jalife, "Electrical turbulence as a result of the critical curvature for propagation in cardiac tissue," *Chaos* **8**, 116–126 (1998).
- ⁸⁸J. Keener, "Propagation and its failure in coupled systems of discrete excitable cells," *SIAM (Soc. Ind. Appl. Math.) J. Appl. Math.* **47**, 556 (1987).
- ⁸⁹J. Keener, "The effects of discrete gap junction coupling on propagation in myocardium," *J. Theor. Biol.* **148**, 19 (1991).
- ⁹⁰A. Panfilov and P. Hogeweg, "Scroll breakup in a three-dimensional excitable medium," *Phys. Rev. E* **53**, 1740 (1996).
- ⁹¹D. Frazier *et al.*, "Stimulus-induced critical point: Mechanism for the electrical initiation of reentry in normal canine myocardium," *J. Clin. Invest.* **83**, 1039 (1989).
- ⁹²G. Moe, W. Rheinboldt, and J. Abildskov, "A computer model of atrial fibrillation," *Am. Heart J.* **67**, 200 (1964).
- ⁹³B. Saxberg and R. Cohen, "Cellular automata models of cardiac conduction," in *Theory of Heart*, edited by L. Glass, P. Hunter, and A. McCulloch (Springer-Verlag, New York, 1991), pp. 437–476.
- ⁹⁴B. Kenneth, R. Laurita, S. Girouard, and D. Rosenbaum, "Modulation of ventricular repolarization by a premature stimulus. Role of epicardial dispersion of repolarization kinetics demonstrated by optical mapping of the intact guinea pig heart," *Circ. Res.* **79**, 493 (1996).
- ⁹⁵M. Vinson, A. Pertsov, and J. Jalife, "Anchoring of vortex filaments in 3d excitable media," *Physica D* **72**, 119 (1993).